MIKOCKI, S.

INCLUSIVE RESONANCE PRODUCTION IN SINGLE-VEE EVENTS IN $\pi^- N$ INTERACTIONS AT 200 GeV

E-580

(Ph.D. Dissertation)

Stanislaw Mikocki

Physics Department
Virginia Polytechnic Institute and State University
Blacksburg, Virginia 24061

(August 23, 1985)

(VPI-EPP-85-4)

(ABSTRACT)

We present results from Fermilab MPS experiment E580 on the reactions $\pi^- N \to V^\circ X$ where V° is K°_S, Λ or $\bar{\Lambda}$ and X are charged particles. Transverse and longitudinal momentum distributions for the V° and for $K^{*\pm}(892)$, $\Sigma^\pm(1385)$, $\Xi^-(1321)$ and $\bar{\Xi}^+(1321)$ are presented. A comparison is made with the prediction of QCD quark counting rules. Evidence for Λ_c^+ is presented.

FERMILAB
LIBRARY

QC 101
.M589

AAB2638

ACKNOWLEDGEMENTS

I would like to thank the E-580 collaboration for giving me the chance to analyse data in this experiment, and especially I would like to thank Dr. John Ficenec for his help, guidance and our seemingly endless discussions. I would like to thank my fellow graduate student Sergio Torres for his help and advice.

I would like to recognize the Institute of Nuclear Physics in Cracow, Poland for support.

I would like to express my deepest admiration and respect to my advisor Dr. W. Peter Trower, for making all this happen. Without his great guidance and patience, I would never have finished this work. I would like to thank him for always being there to support me and for his understanding and encouragement through the difficult times. It has been a great pleasure to know him and I will always be indebted to him.

Finally, I would like to thank my wife and son for their patient understanding, love and encouragement through all these years. As a small token of my deepest appreciation, I dedicate this work to them.

This was supported in part by NSF-PHYS 8020441/8317588.

INTRODUCTION

Currently leptons and quarks are thought to be the elementary constituents of matter. Leptons exist as free particles while quarks, the assumed constituents of hadrons, have never been isolated. Leptons are the electron, its neutrino ν_e, the muon and its neutrino ν_u, the recently discovered τ and its postulated neutrino, ν_τ. There are five known quarks - u (up), d (down), s (strange), c (charm) and b (bottom) - and a putative sixth quark, t (top). These quarks and leptons are said to have different flavors.

In the standard model the interactions between quarks and of quarks and leptons is described by a renormalizable non-abelian gauge field theory [1] whose symmetry group is $SU_c(3)xSU_L(2)xU_{em}(1)$. The $SU_c(3)$ group applies to the strong interaction of colored quarks mediated by an octet of massless colored gauge bosons: gluons. Color, the charge of strong interactions, causes this theory to be called quantum chromodynamics (QCD). Electroweak interactions described by the spontaneously-broken symmetry group $SU_L(2)xU_{em}(1)$ allow interactions of quarks and leptons with four gauge bosons, the photon and the massive $W^\pm$ and Z° weak bosons. This model unifies quantum electrodynamics (QED) with weak V-A theory and has successfully passed all experimental tests, the most spectacular of which was the $W^\pm$ and Z° discovery at the predicted masses.

The quark hypothesis [2] was introduced to describe hadron properties. Quarks have color, flavor, spin 1/2 and fractional electric charge, -1/3 or +2/3 e. The mediating gluons have two colors and spin

1, but no charge, flavor or baryon number. Mesons are a bound quark-antiquark and baryons are three bound quarks.

Experiments that probed nucleon structure by electron scattering showed protons had point-like constituents called 'partons' [3] which were quickly associated with quarks. Valence quarks give hadrons flavor while virtual quark-antiquark pairs in the "sea" are created by vacuum polarization of the color field. Virtual gluons in the sea are the color force field quanta exchanged between quarks.

QCD has the important property of local non-abelian gauge symmetry, asymptotic freedom. Asymptotic freedom states that for quark-quark collisions the effective strong interaction coupling constant, α_s, weakens with momentum-transfer (i.e. at small distances). Free quarks, gluons and colored bound states have never been observed. Therefore, it has been assumed that quarks and gluons are confined in hadrons. At small distances, perturbative QCD successfully predicts the properties of hard processes such as e^+e^- annihilation into hadrons, deep inelastic lepton scattering and large tranverse momentum (P_T) hadron-hadron collisions.

The collision of two hadrons usually results in multiparticle production limited in P_T with respect to the collision axis. These forward-backward jets, which account for the bulk of the hadronic cross section, evolve in some way from the constitutent quarks and gluons of the incident colliding hadrons. In particular the longitudinal momentum (X_F) distribution of fast hadrons with low-P_T have been the subject of quark-parton models [4], one class of which, the so-called quark

counting rules (QCR), seems successful.

QCR predict the power n of $d\sigma/dX_F = A(1-X_F)^n$ for inclusive distributions observed in fragmentation processes as $X_F \to 1$. n is the number of spectator quarks involved in the fragmentation. n differs if quark or gluon exchange is dominant or if the sea quarks are among the spectators, and it depends on the details of how all this is done. Quark exchange, which would produce long range correlations between the colliding hadron fragmentation regions, has not been observed at significant levels. Soft gluon exchange would leave the initial hadron quark unperturbed and so the quark jet fragments are attributed to the observed fast hadron. The initial QCR prediction of $n = 2n_s - 1$, where n_s is the least number of spectator valence and sea quarks from the beam hadron, disagrees with experiment. If only valence quarks are counted as spectators, then $n = 2n_s^v - 1$, which, although more sucessful, fails to describe the observed steepness of baryon spectra in meson fragmentation.

Recently, QCR have been developed using lowest-order QCD [5] where the dominant diagrams give $n = 2n_H + n_{PL} - 1$. n_H is the number of initial hadron spectator quarks and n_{PL} is the number of spectators emerging from point-like bremstrahlung interactions. The three QCR diagrams for $\pi^- \to \Lambda$ are seen in Fig. 1.1.

Although the latter QCR agree rather well with the data [4], several diagrams usually contribute to one process. To naively expect the smaller n terms to dominate at high X_F is not justified unless the relative normalization is known. The success of QCR can neither confirm

nor contradict other models, because the freedom in choosing dominant diagrams allows confrontations with QCR to be avoided. Nevertheless, QCR provides useful estimates of spectra where no data exists and a systematic framework in which to compare fragmentation data.

The fourth flavor quark, charm, was postulated to restore symmetry between the number of quarks and leptons then known [6]. More compelling was the GIM mechanism [7] in which charm was introduced to explain the suppression of strangeness-changing neutral currents. Two independent groups discovered a narrow vector meson state, the $\psi/J(3097)$ [8], now established to be a charm-anticharm bound state. The first particle to be observed with non-zero charm was the D(1870) discovered in $K\pi$ and $K\pi\pi$ decay products [9]. With a fourth quark, SU(4) hadron spectroscopy was developed [10], the lowest-lying charm states of which are listed in Table 1.1.

The charm quantum number is conserved in strong and electromagnetic interactions so the lowest-lying charm states decay weakly with lifetimes $\sim 10^{-13}$ seconds. The relative strengths of charm decays are estimated from their couplings suppressed by factors of $\cos\theta_c$ and $\sin\theta_c$ in the transition; $\theta \approx 13°$ is so-called Cabibbo angle. Ignoring phase space and dynamics, the predicted relative rates [11] are,

$$c \to s u \bar{d} \sim 3 \cos^4\theta_c \qquad c \to s u \bar{s} \sim 3 \sin^2\theta_c \cos^2\theta_c$$

$$c \to d \bar{d} u \sim 3 \cos^2\theta_c \sin^2\theta_c \qquad c \to d u \bar{s} \sim 3 \sin^4\theta_c$$

$$c \to s \ell^+ \nu_\ell \sim \cos^2\theta_c \qquad c \to d \ell^+ \nu_\ell \sim \sin^2\theta_c$$

while the selection rules are listed in Table 1.2 [12]. Since $\cos^2\theta_c \gg \sin^2\theta_c$, the transition proportional to $\cos^2\theta_c$ is called a

Cabibbo allowed, whereas Cabibbo suppressed is proportional to $\sin^2\theta_c$.

Cabibbo-allowed decays of non-strange charm particles produce a single strange particle, a potent signal for charm. Searching for charm particles can involve detecting short-lived particles with high spatial resolution vertex detectors and thus measuring lifetimes; looking for prompt leptons from semi-leptonic decays and thus measuring the prompt leptons yield or providing a tag so the other member of the charm-anticharm pair can be sought; and hunting for narrow enhancements in effective mass distributions where detectability in the fierce combinatorial backgrounds is made possible by particle identification, limiting multiplicity and/or selecting a priori a region of phase space (e.g. the diffractive or high-P_T region).

A decade of experimental searches for charm particles [13] has provided substantial information about charm mesons but scant information about charm baryons: only the Λ_c^+ is well studied; of the strange-charm baryons the A^+ and T^0 are observed in one experiment and the Σ_c has been reported in $\Sigma_c^{++} \to \Lambda_c^+\pi^+$ and $\Sigma_c^+ \to \Lambda_c^+\pi^0$.

Most hadro-produced charm information [14] comes from center of mass energies, $s^{\frac{1}{2}} \sim 20$ GeV (FNAL/SPS) and $s^{\frac{1}{2}} \sim 60$ GeV (ISR). Since most experiments are sensitive in a limited kinematic range, the extrapolation to the whole of phase space is highly model dependent and so experimental cross sections from different experiments are difficult to compare. Also the cross section dependence on the atomic number A is unknown. Further, banching ratios used in cross section calculations must be scrutinized. For example, the first ISR total charm production

cross section for hadronic final states (~1mb) was an order of magnitude larger than that for detected leptons. Subsequent data resolved this conflict with the current cross sections being 100-500 μb. At FNAL/SPS energies, the D meson cross sections are ~ 10-30 μb with incident pions being as effective as protons. Λ_c^+ cross sections range from 3 to 100 μb.

Further, hadron-proton cross section (σ_P) is related to that of the hadron-nucleus (σ_A) by $\sigma_A = A^\alpha \sigma_P$, where the data strongly favors $\alpha = 1$ consistent with perturbative QCD models and in contradiction to diffractive models which predict $\alpha = \frac{2}{3}$. Further, α may also depend on X_F and P_T.

The hadro-production cross section, $(d\sigma/dX_F) \sim (1-X_F)^n$, was believed to be produced centrally, n ~ 5. However, the first ISR results showed the Λ_c^+ produced forward with a flat X_F distribution of n ~ 0.4. The D meson at FNAL/SPS energies was also produced forward with n ~ 2. For pions a recent 360 GeV/c $\pi^- p$ experiment indicates two X_F components; one central with n = 6 and the other forward with n = 1, while all other experiments observe leading components. Direct lepton experiments favor n ~ 5-6 for proton interactions and a two component distribution for pions with n ~ 6 and 0.5. In contrast all hadro-production experiments fit an $\exp(-aP_T^2)$ distribution with a ~ 1.1 $(\mathrm{GeV/c})^{-2}$ over the whole energy range.

No theoretical model completely explains the hadronic charm production data. These models fall into three catagories depending on the assumed source of charm: flavor creation, flavor excitation and

intrinsic charm. The flavor creation model has charm created in gluon fusion ($gg \rightarrow c\bar{c}$) or quark-antiquark annihilation ($q\bar{q} \rightarrow c\bar{c}$), predicts cross sections of a few μb at $s^{\frac{1}{2}} \sim 20$ GeV and ~ 100 μb at 60 GeV and is central, increasing at $X_F \sim 0$ with energy. The flavor excitation model assumes a charm quark from the sea excited by $gc \rightarrow gc$ and $qc \rightarrow qc$, strongly depends on the specific parameters and evaluation of the charm sea but describes rather well the forward charm production and the cross section increase for pp interactions between FNAL/SPS and ISR energies. The intrinsic charm model has a valence-like intrinsic $c\bar{c}$ component which, in contrast with $c\bar{c}$ pairs from the sea, exist for a long time and are associated with bound state hadron dynamics. This latter model predicts diffractive-like forward production of charm baryons and anti-charm mesons with cross sections proportional to log(s) and $A^{\frac{2}{3}}$.

An effective way to search for new narrow resonances is to probe a definite final state such as e^+e^- or $\mu^+\mu^-$ ($\rho,\omega,\phi,J/\psi,T$) where these di-lepton resonances have restricted spin-parity, $J^P = 1^-$. By this technique the unexpected J/ψ and T resonances were discovered. The goal of the experiment E580 (Arizona/Fermilab/Flordia State/Notre Dame/ Tufts /Vanderbilt/Virginia Tech) was to extend this technique to the reactions,

$\pi^-N \rightarrow \Lambda\bar{\Lambda}X$	$I = 0$	$J^P = 0^+,0^-,\ldots$
$\rightarrow \Lambda\bar{\Lambda}\pi^{\pm}+X$	$= 1$	$= 1^+,2^+,\ldots$
$\rightarrow K^0_sK^0_sX$	$= 0,1$	$= 0^+,2^+,4^+,\ldots$
$\rightarrow K^0_sK^0_s\pi^{\pm}X$	$= 1,2$	$= 1^+,1^-,\ldots$

at high mass. E580 was carried out in spring 1980 and some results have

been published [15].

Here I report the analysis of data where only one V° was reconstructed. In Chapter 2 I describe the E580 detector, trigger and data analysis. I study strange particle [K°_{S}, Λ, $\bar{\Lambda}$, Ξ^{-}, $\bar{\Xi}^{+}$] and resonance [$K^{*\pm}(892)$, $\Sigma^{\pm}(1385)$] production and compare with QCR in Chapter 3. In Chapter 4 I give the evidence for the production of the charm baryon $\Lambda_{c}^{+}(2282)$. A summary appears as Chapter 5.

THE EXPERIMENT

2.1 Apparatus: Experiment E580 triggered on reactions $\pi^- N \rightarrow V^\circ V^\circ X$ where V° was a K°_S, Λ and $\bar{\Lambda}$ while X were charged particles. The experiment was carried out in the 200 GeV/c π^- M6W beam line using the Fermilab Multiparticle Spectrometer (FMPS), configured as seen in Fig. 2.1.1. Not shown upstream of target was the system of beam counters and detectors. Two in-beam counters and a hole counter veto defined the beam. Three proportional wire chambers (PWC) modules (BA1, BA2 and BA3) located upstream (-28, -16 and -0.87 m) from the target provided the beam direction. The BA1 module had 2 PWC planes with 128 wires, BA2 had 3 PWC planes with 192 wires and BA3 had 3 PWC planes with 96 wires.

The "active" target consisted of 20 individual plastic scintillators (Pilot-B with $\rho \sim 1.032$ g/cm^3) where the dimension of each was 3.172±0.003 cm square by 0.621±0.006 cm thick. Each counter was wrapped in heat shrink tubing and aluminum and had a center-to-center spacing of 12.9 mm. The target center was located at -4.72 m from the front face of the magnet defined as z = 0. For each trigger the pulse height of each counter was digitized and recorded. The active target provided longitudinal primary vertex location within 12.9 mm.

Directly downstream of the target were 6 PWC planes (A station) with 2x(0°), 2y(90°) and a u-v pair at ±45° to verticle. The x and y pairs were 1/2 mm effective spacing. Downstream of the A-station was a decay region filled with helium gas to reduce interactions where neutral strange particles (V°) materialized into charged tracks. Next 5 PWC

planes (B',B), 4x and 1y fronted the spectrometer magnet made of superconducting ferrite which produced a 16.9 kG centrally homogeneous field at maximum excitation of 180 amperes. The magnet, whose aperture was 122 cm in x by 72 cm in y and 256 cm in z, imparted a 697 MeV/c P_T change to each charged particle. Mounted inside the magnet were an x-y pair of planes, the C station.

Downstream of the magnet were 5 PWC planes (D) with 2x, 1y and a u-v pair at $\pm 15^\circ$ to the vertical, followed by a nitrogen-filled, atmospheric Cherenkov counter (C_B) whose 30 cells provided particle identification. Figure 2.1.2 shows the Cherenkov mirror segmentation while Table 2.1.1 summarizes the parameters of this counter. Next were 8 large magnetostrictive spark chamber modules (E,F) constructed in two-gap units with stretched aluminum wire electrodes. Each unit had one gap with x electrodes and one formed with wires tilted at arctan $\theta = \pm 0.1$ to the vertical. Each module had three magnetostrictive readout wands - x, y, u or v- and had a sensitive area of ~ 2.4 x 1.2 m (E) or ~ 3.6 x 1.8 m (F). Interspaced in the the beam region between the last 3 spark chambers were 3 PWC planes (F') with 1x, 1y and 1v(45°).

2.2 <u>Trigger</u>: A small scintillator counter after the Cherenkov counter signaled the disappearance of a beam particle. The trigger then counted the tracks (i.e. clusters of "hits") in the A_u and A_v PWC planes before the decay volume, and B'_x, $B'_{x'}$, C_x, C_y, D_x, D_y and $D_{x'}$ after the decay volume. The $V^\circ V^\circ$ trigger required a charged particle multiplicity increase of 4 ± 1 in the decay volume, with the multiplicity in at least

three of the C/D planes equal to that measured in the B' station, and a primary charged multiplicity, measured before the decay volume, ≤ 5. The pulse height of each scintillation target counter were fast summed and used in the trigger to determine if the interaction had taken place in the target.

2.3 Data: The average beam intensity was - 6×10^5 π^-/1sec over a 400 hour run which resulted in a total data taking flux of 1.2×10^{10} π^- giving 1.2×10^6 two-Vee triggers. An additional 3×10^5 triggers of noninteracting beam, elastic scattering (1 pion), diffractive (3 pions) and one-Vee plus pion events were taken for diagnostic purposes and to verify the mass and momentum scales. All triggers were passed through a pattern recognition program (TEARS). A noninteracting beam was used for momentum calibration, alignment and program tune-up. TEARS found straight track segments upstream and downstream of the magnet which it matched at the magnet midplane. Upstream segments, which did not have hits in the A-chambers were candidates for decay legs from neutral Vees. Very loose cuts were made on the Vee vertex in decay volume and on the Vee mass. Next, a global three dimensional spline fit was made using a detailed map of the magnetic field to obtain the momentum and angles for each track. Each V^0 was tested with three hypotheses: K^0_S, Λ and $\bar{\Lambda}$. For the best hypothesis the K^0_S mass distribution had a full width at half maximum (FWHM) 14 MeV/c^2, while the Λ and $\bar{\Lambda}$ distributions had 5 MeV/c^2 (FWHM). Finally, track parameters were varied in fits constrained to the Vee mass and the Vee decay vertex. Cuts were made requiring the fit

probability to be greater than 10^{-5}. Of the ~ 70,500 two-Vee events that survived 62% were $K^o_S K^o_S$, 16% were $K^o_S \Lambda$, 13% $K^o_S \bar{\Lambda}$, 8% $\Lambda\bar{\Lambda}$ and 1% $\Lambda\Lambda$ or $\bar{\Lambda}\bar{\Lambda}$. Here we present results using ~25% of the data sample where only one V° was reconstructed: 43,299 K^o_S, 7,188 Λ and 6,294 $\bar{\Lambda}$.

The primary interaction vertex was found by two methods. In the first method, direct track vertex, a least square fit of all tracks to a point was made excluding beam and V° tracks. If the chi-squared per degree of freedom (χ^2/DOF) was $\geq$ 30, the poorest fitting track was deleted and the fit repeated. If the vertex was found, it had to lie within 5σ from the target boundaries. In the second method, the scintillator target counter ADCs were examined for abrupt increases in the pulse height, with up to three abrupt increases allowed. This gave the z-coordinate of the interaction vertex without ambiguity if only one abrupt increase was detected. Using the beam track, the x and y coordinates at the z interaction point were computed. If both methods gave a solution, the z-coordinates were compared and if the difference was $\geq$ twice the sum of the z-coordinate errors the direct track vertex was rejected. Otherwise, the weighted average of the two solutions was computed.

In the subsequent physics analysis cuts were made to eliminate false tracks found in pattern recognition as well as secondary interactions. We require:

1. The primary vertex be within 5σ of the measured limits of the target; and the total visible momentum (V° plus tracks) $\leq$ 230 GeV/c.
2. The V° points to the primary vertex ($\chi^2 < 20$); the decay vertex be

within $\pm 3\sigma$ in the z direction of the decay region; differences in slope of the V° legs (Θ) small in the x-z or y-z view resulted in the V° being discarded ($\Delta\Theta_x < 0.5$ or $\Delta\Theta_y < 0.15$ mrad); and differences in leg intercept (b) small in the x-z or y-z view resulted in the V° being discarded ($\Delta b_x < 0.15$ or $\Delta b_y < 0.15$ cm).

3.The track momentum be $\leq$ 210 GeV/c or else it was discarded; the slope and intercept differences of V° legs and primary tracks too small in the x-z or y-z view resulted in the primary track being discarded ($\Delta\Theta_x \leq 0.9$ mrad and $\Delta b_x \leq 0.25$ cm or $\Delta\Theta_y \leq 0.4$ mrad and $\Delta b_y \leq 0.15$ cm); and any two primary track slope and intercept differences too small in the x-z or y-z view resulted in one track being discarded ($\Delta\Theta_x \leq 0.4$ mrad and $\Delta b_y \leq 0.20$ cm or $\Delta\Theta_y \leq 0.25$ mrad and $\Delta b_y \leq 0.12$ cm); and a track χ^2 relative to the vertex was $\leq$ 35 or the track was discarded. The cuts reduced the event sample to 25,565 K°_S, 3,999 Λ and 3,041 $\bar{\Lambda}$.

All direct charged tracks were assumed to be pions, except for $\Lambda^+_c(2282)$ analysis.

In the next chapters we study particle production by examining invariant mass distributions for given decay modes and by fitting the X_F and P_T^2 distributions. The backgrounds for these distributions are obtained from mass side-bands of the system under study. The X_F distributions are corrected for acceptance, but the P_T^2 distributions are not. The acceptances are estimated using Monte-Carlo generated events for a given reaction with a flat X_F distribution and P_T^2 distributed as $\exp(-bP_T^2)$, unless noted otherwise with b = 2.5 $(\mathrm{GeV/c})^{-2}$. These events

were propagated through the FMPS using computer codes that take into account the detector geometry and the restricted decay region for the V°. In performing the fits, the χ^2 contribution of each histogram bin is based on the difference between the number of events in the bin and the integral of the fitted function over that bin interval. The fits were obtained using a χ^2-minimizing program (MINUIT, CERN Library) whose error in the fit parameters was determined by noting the parameter variation which increased χ^2 by one.

2.4 Particle Identification: A charged particle moving through a dielectric radiates a small amount of energy if its velocity is greater than the phase velocity, c/n, of light in that medium. The Cherenkov light cone angle for a particle moving at a velocity $\beta = v/c$ in a refractive medium of index n is $\cos\theta = 1/n\beta$. At $\theta = 0$ is the momentum threshold, P_{th}, at which the particle begins to produce light: $P_{th} = m/(n^2-1)^{\frac{1}{2}}$. In Fig. 2.4.1 we present the possibility of identification of particles using Cherenkov counter data with an identification algorithm [16]. The momentum thresholds for pion, kaon and proton define four, distinct momentum regions. In the first, charged particles below the pion momentum threshold (T_π) will not produce Cherenkov light, and thus could be a pion, kaon or proton (π/K/p low). Similarly, a momentum above T_π and below the kaon threshold (T_K) would be a pion if it produced light or ambiguously (K/p) if there was no light. In the third region a particle momentum between T_K and the proton threshold (T_p) would be a proton if no light was detected and

ambiguous π/K if light was seen. Particles with momentum above T_p are ambiguously $\pi/K/p$. The region labled 'e' is that of tracks with momentum below threshold for pions that gave light, they can be electrons or can result from tracking inefficiencies or identification algorithm inefficiency. Finally, in the region above threshold for protons, where all tracks should emit light, there is a small fraction of tracks which due to the inefficiency of the detector, Cherenkov algorithm or spurious track finding are not possible to identify because no light was detected. The average inefficiency in particle identification was determined to be ~20% by comparing the particle assignment of the Cherenkov counter for known masses of V legs based on independent reconstruction of K^o_S, Λ and $\bar{\Lambda}$. Cherenkov particle identification was only used in the Λ_c analysis (Chapter 4), where we assume all ambiguities involving pions as pions and protons are particles with momentum between 20.0 GeV/c and 38.8 GeV/c with no light detected.

3.1 K^o_s and $K^*(892)$ Production: In Fig. 3.1.1 we plot the K^o_s $X_F(dN/dX_F)$ distribution, where a fit over $0.2 \leq X_F < 0.8$ to the distribution $(1-X_F)^n$ gives $n = 1.66\pm0.05$ with $\chi^2/DOF = 9.51/13$. QCR predict an $A(1-X_F)^3 + B(1-X_F)^1$ distribution, whose fit to our data yields $A/B = 1.67\pm0.13$ with $\chi^2/DOF = 15.3/13$.

The K^o_s P_T^2 distribution, seen in Fig. 3.1.2, fits to a sum of two exponentials with slopes 2.11 ± 0.33 and 4.98 ± 0.53 $(GeV/c)^{-2}$ while those for three X_F regions fit to a single exponential with 2.55 ± 0.06 $(0.3 \leq X_F < 0.5)$, 2.74 ± 0.13 $(0.5 \leq X_F < 0.7)$ and 3.09 ± 0.33 $(0.7 \leq X_F < 0.1)$ indicating that the P_T^2 slope gets somewhat steeper as X_F increases. This behavior would even be stronger if the data were acceptance corrected in this variable.

The fits to the inclusive mass distributions for $K^o_S\pi^-$ and $K^o_S\pi^-$ with $X_F > 0$ and all P_T^2, seen in Fig. 3.1.3, show more $K^{*-}(892)$ than $K^{*+}(892)$; but the fraction of $K^o_s\pi^-$ that are K^{*-} and the fraction of $K^o_s\pi^+$ that are K^{*+} are relatively the same. We fit a P-wave Breit-Wigner [15] for the $K^*(892)$ and background of $A(M-m_o)^B\exp\ [-C(M-m_o) - D(M-m_o)^2]$ where M is the $K\pi$ mass, m_o the threshold mass and A, B, C, D are fit parameters. The fitted mass (MeV/c^2), full width at half-maximum (MeV/c^2) number of resonances events and χ^2/DOF was 888 ± 2, 64 ± 8, $2{,}706\pm313$ and 30.8/41 for the K^{*-} and 889 ± 3, 70 ± 12, $1{,}813\pm309$ and 50.5/41 for the K^{*+}. The $X_F(dN/dX_F)$ acceptance corrected distributions for the K^*, seen in Fig. 3.1.4, are background subtracted. This

background was obtained from 40 MeV/c^2 mass side-bands in the $K\pi$ system, above and below the $K^*(890)$ mass band. Using the usual parameterization $(1-X_F)^n$, we obtain $n = 0.86\pm0.20$ for K^{*-} with $\chi^2/DOF = 2.6/2$ and $n = 1.86\pm0.36$ for the K^{*+} with $\chi^2/DOF = 1.1/2$. The X_F distribution ratio is free of acceptance assumptions and was fit to $R_o(1-x)^n$ with $n = 1.05\pm0.35$, $R_o = 0.98\pm0.16$ and $\chi^2/DOF = 2.4/3$.

The K^* production P_T^2 dependence , seen in Fig 3.1.5, was parameterized by $e^{-bP_T^2}$. The fit gave $b = 2.72\pm0.28$ for K^{*-} and $b = 2.50\pm0.27$ for K^{*+} over the interval $0 \leq P_T^2 \leq 1.2$ $(GeV/c)^2$ with $\chi^2/DOF = 12.71/4$ and $10.98/4$, respectively.

We find $R(K^{*+}/K_S^o)$ of 0.071 ± 0.012 and $R(K^{*-}/K_S^o)$ of 0.106 ± 0.012. If K^{*o} and $\bar{K}^{*o}$ are produced in proportion to K^{*+} and K^{*-}, then our K^*/K_S^o ratio of ~ 35% is consistent with those of bubble chamber experiments [17].

3.2 <u>Λ, $\Xi(1321)$ and $\Sigma(1385)$ Production</u>: In Fig 3.2.1 we plot the Λ and $\bar{\Lambda}$ $(X_F dN/dX_F)$ fit over the interval $0.15 \leq X_F < 0.8$ giving $n = 1.97\pm0.11$ $(\chi^2/DOF=6.8/11)$ for Λ and $n = 1.96\pm0.13$ $(\chi^2/DOF=11.5/11)$ for $\bar{\Lambda}$. The $R(\bar{\Lambda}/\Lambda)$ at $X_F \sim 0$ is ~ 0.6, indicating a possible target proton fragmentation contamination. For $0.1 \leq X_F < 0.65$, $R(\bar{\Lambda}/\Lambda) \sim 0.78$, and for $X_F \geq 0.65$ $R(\bar{\Lambda}/\Lambda)$ increases above 1. The same behavior of the $\bar{\Lambda}/\Lambda$ ratio was observed in the experiment E-580 in the data sample $K_S^o\Lambda/K_S^o\bar{\Lambda}$ [15].

A single exponential fit to the P_T^2 distributions for $X_F > 0$ with $b = 2.46\pm0.03$ for Λ and with $b = 2.57\pm0.07$ for $\bar{\Lambda}$ is seen in Fig. 3.2.2.

For $0.3 \leq X_F < 0.5$ and $0.5 \leq X_F < 0.7$, the fitted slopes are 2.64±0.16 and 2.32±0.32 for Λ, and 2.42±0.19 and 2.07±0.39 for $\bar{\Lambda}$.

The $\Xi(1321)$ is present in the $\Lambda\pi^-$ and $\bar{\Lambda}\pi^+$, in Fig. 3.2.3. A fit to a Gaussian resonance with standard deviation σ and a quadratic background, $A(M-m_o) + B(M-m_o)^2$ yielded 48±10 Ξ^- events with $M = 1322.1\pm0.3$ MeV/c² and $\sigma = 1.2\pm0.3$ MeV/c² (χ^2/DOF~76/75); and 33±10 $\bar{\Xi}^+$ events with $M = 1322.2\pm0.4$ MeV/c² and $\sigma=1.3\pm0.5$ MeV/c² (χ^2/DOF ~ 101/75). A fit to the combined distribution gave 72±15 events with $M = 1322.2\pm0.3$ and $\sigma = 1.1\pm0.3$ MeV/c² (χ^2/DOF = 75/75). Our mass is slightly higher than the accepted 1321.52±0.13 MeV/c² [13] and our width is consistant with our mass resolution of 1.5 MeV/c² at the Ξ mass.

A fit to the acceptance corrected X_F distribution, seen in Fig. 3.2.4, gave $n = 2.21\pm1.95$ for Ξ^- and $n = 8.40\pm9.09$ for $\bar{\Xi}^+$, showing that the latter may be produced more centrally. The single exponential fit to the P_T^2 distribution, seen in Fig. 3.2.4, gives $b = 2.81\pm1.05$ and 2.08±1.06, respectively, for Ξ^- and $\bar{\Xi}^+$. In Fig. 3.2.5, we plot $\Lambda\pi^-$ and $\bar{\Lambda}\pi^+$ mass combinations in 20 MeV/c² bins and observe signals from the $\Xi(1321)$ and $\Sigma(1385)$. In Fig. 3.2.6, the $\Sigma^+(1385)$ is seen in $\Lambda\pi^+$ but the $\bar{\Sigma}^-(1385)$ is only marginally present in $\bar{\Lambda}\pi^-$ and an unexpected dip is observed at the low mass, ~1320 MeV/c². We fit a Gaussian to the $\Xi(1321)$, a Breit-Wigner to the $\Sigma(1385)$ and a $A(M-m_o)^B \exp[-c(M-m_o)^D]$ background, with masses fixed at the accepted values [13]. The $\Xi(1321)$ widths taken from the previous fit and the accepted $\Sigma(1385)$ widths were increased by 5 MeV to account for our mass resolution, $\sigma = 2$ MeV/c² at the Σ mass. From these fits we have 219±50 $\Sigma^-(1385)$, 154±46 $\Sigma^+(1385)$,

84±40 $\bar{\Sigma}^-(1385)$ and 64±42 $\bar{\Sigma}^+(1385)$ events. We observe that the strange antibaryons are produced substantially weaker than the strange baryons. A fit to the X_F and P_T^2 distributions, seen in Fig. 3.2.7, for the more statistically significant $\Sigma^-(1385)$ and $\Sigma^+(1385)$ gave n = 1.44±0.41 (χ^2/DOF~0.04/3) and b = 3.87±2.35 (χ^2/DOF~0.66/4) for $\Sigma^-(1385)$, and n = 3.81±2.16 (χ^2/DOF~0.07/2) and b = 2.90±1.39 (χ^2/DOF~0.99/4) for $\Sigma^+(1385)$.

3.3 Comparison with QCR and Other Data: In Table 3.3.1 we summarize our fits to X_F distributions together with QCR predictions [5]. Our experimental n values are systematically lower than those QCR predict but are consistent within our experimental errors except for K^{*+}. Thus, we conclude that valence quarks play a significant role in strange particle production since particles produced without a valence beam quark have a steeper X_F distribution than particles with the initial valence beam quark.

Recent E580 results [15] for $K^*(892)$ from 2V° ($\pi^- N \rightarrow K_S^o K_S^o + X$) data found n = 0.64±0.12 for K^{*-}; n = 2.76±0.32 for K^{*+}; and for the K^{*+} to K^{*-} ratio R_o = 0.89±0.19 and n = 2.24±0.34. For $\bar{K}^{*o}(\bar{d}s)$ and $K^{*o}(\bar{s}d)$ production by 175 GeV π^- on a beryllium [18] a fit to the invarient X_F distribution found n = 0.69±0.10 ($0.1 \leq X_F \leq 0.9$) and 0.59±0.13 ($0.3 \leq X_F \leq 0.9$) for K^{*o}; 1.82±0.27 ($0.1 \leq X_F \leq 0.9$) and 1.47±0.51 ($0.3 \leq X_F \leq 0.9$) for $\bar{K}^{*o}$ and for $R(\bar{K}^{*o}/K^{*o})$ R_o = 0.86±0.08 and n = 1.11±0.27 consistent within errors to $R(K^{*+}/K^{*-})$ at X_F~0. The Fermilab Single Arm Spectrometer [19] studied K^+ and K^- production at

100 GeV/c and 175 GeV/c at numerous X_F and P_T^2 values for $0.12 \leq X_F \leq 0.94$ and $0.15 \leq P_T^2 \leq 0.75$ GeV/c. Their results were $n = 2.06 \pm 0.25$ for $\pi^- \to K^-$ ($X_F < 0.5$) and $n = 2.85 \pm 0.22$ for $\pi^- \to K^+$ at 175 GeV/c and 1.84 ± 0.30, 1.76 ± 0.10 for K^-, K^+ respectively at 100 GeV/c. The inclusive spectra K_S^o, Λ and $\bar{\Lambda}$ from 200 GeV/c π^- incident on a beryillium target at $p_T = 0$ were studied [20]. Results were $n = 0.262 \pm 0.013$ for K_S^o and 3.09 ± 0.013 for Λ and $\bar{\Lambda}$. The K_S^o and $K^\pm$ distributions have values of n which are generally intermediate between the K^{*+} and K^{*-} values, as expected if resonance decay is significant.

Data on strange baryon production from π^- beam are very limited. Using the $K_S^o\Lambda/K_S^o\bar{\Lambda}$ sample of data, experiment E-580 found $n = 5.8 \pm 1.7$ from the combined X_F distribution $\Sigma^\pm(1385) + \bar{\Sigma}^\pm(1385)$ and $n = 6.7 \pm 0.3$ for $\Xi^-(1321) + \bar{\Xi}^+(1321)$ [15]. Both fragmentation processes $K^- \to p$ and $\pi^- \to \Sigma^{*+}$ have the same QCR prediction of $n = 4$. Using data from 100 GeV/c and 175 GeV/c incident K^- beam, the Fermilab Single Arm Spectrometer found $n = 3.86 \pm 1.10$ for $0.2 \leq X_F \leq 0.7$ and $0.3 \leq P_T^2 \leq 1.0$ GeV/c [21] which is in agreement with our value for the Σ^{*+}.

Our results confirm the conclusion of the comprehensive comparison of the experimental results with QCR [4], that QCR give a resonably rough estimate of n values, but the data seems to exhibit systematic differences between various processes of the same class, presumably related to spin and flavor effects.

3.4 <u>Cross Sections</u>: The cross section is defined as $\sigma = SN_o/A'A$. N_o is the number of observed events, A the spectrometer acceptance, A' a

correction for inefficiencies not included in the acceptance, and S is the microbarn ($1b = 10^{-24} cm^2$) equivalent of the experiment (i.e. the cross section for 1 event) calculated as $S = (N_t N_b)^{-1}$ $= (328.27 \times 10^2 \text{ events}/\mu b)^{-1}$, where N_t is the number target particles, $6.02 \times 10^{23}/g \times [12.80(\text{scint.}) + 0.548(Al) + 2.232(\text{tape})g/cm^2]$ or $93.79 \times 10^{23}/cm^2$, and N_b is the effective beam (the number of beam tracks corrected for dead-time) or 3.5×10^9. The acceptance for the experiment is a product of several factors: the geometrical acceptance or probability that particles in an event will traverse the magnet and chambers, the probability that V° will decay within the helium-filled decay region, the trigger efficiency, and the probability that software will properly reconstruct the event. Included in A' is a correction for the branching fractions involved in a given decay mode and other corrections not included in A. The experiment was designed to trigger 2-V° events and we expect that the trigger efficiency for 1-V° events is substantially lower in comparison to 2-V° events. True 1-V° events could satisfy the 2-V° trigger requirements. Two sources of this mimic of 2-V° triggers are the interections of produced tracks between A and B' and clustering of tracks in A chambers. Multiple hits on adjacent wires in A would be called one track by the trigger. As these tracks separate in B',B,C,D they would be called multiple tracks. Using the different models for the trigger, we estimated that the trigger for 1-V° events was ~ 4 times lower relative to 2-V° events. Independently, it was found that trigger efficiency for 2-V° events was 0.40±0.04. We calculated the expected ratio of $K^o_S K^o_S$ to single K^o_S events from measured

bubble chamber cross sections at 250 GeV/c [22] using our estimated acceptances. The expected ratio, 0.29±0.16, is in good agreement with the experimental value 0.25. As an additional consistency check of 2-V° and 1-V° data, we compared the cross sections for the diffractive dissociation processes in the $K^o_S K^o_S$ and K^o_S samples (Appendix A).

In Table 3.4.1 we summerize the calculated cross sections for different observed states assuming a trigger efficiency of 0.10±0.04, a software acceptance of 0.40±0.04 and current accepted branching fraction [13]. The geometrical and decay volume acceptances were estimated using Monte-Carlo generated events for a given reaction. The trigger dependent cross section represents the forward cross section for the given state, with only one V° in final state and with low charge multiplicity. These cross sections are not real inclusive cross sections because they do not contain the part of cross section from the events with 2-V° and more. To estimate the total inclusive cross sections for the produced states decaying into $V^o\pi^{\pm}$ it is necessary to determine our cross section normalization. We take the cross section measured in a hydrogen bubble chamber at 200 GeV/c π^- [23]: 3.74±0.24 mb, 1.53±0.12 mb and 0.43±0.06 mb for K^o_S, Λ and $\bar{\Lambda}$, respectively. The correction for an additional observed pion was taken into account by the relative acceptance V° and $V^o\pi$ for a given state. The cross sections obtained are seen in the last column of Table 3.4.1.

Other data on inclusive strange resonance production in high energy πN interactions are rather limited. In 175 GeV/c π^-Be interactions, the inclusive cross section for $0 \leq X_F \leq 1.0$ is determined to be 610±20±6 μb

and 380±20±6 μb for $K^{*o}(892)$ and $\bar{K}^{*o}(892)$ respectively [18]. We conclude that is no difference in the production of neutral and charged components of $K^{*}(892)$ in π^- interactions. $K^{*\pm}$ production was observed in π^+p and pp interactions at 147 GeV/c [17]. In π^+p interactions the reported cross sections are 1300±200 μb and 700±200 μb for K^{*+} and K^{*-} respectively, and 1500±300 μb for K^{*+} and 1200±300 μb for K^{*-} in pp interactions. Using the $K^o_S\Lambda/K^o_S\bar{\Lambda}$ sample, experiment E580 reports the total inclusive cross sections 41±4 μb and 23±8 μb for the production $\Xi^- + \bar{\Xi}^+$ and $\Sigma^{*\pm}(1385) + \bar{\Sigma}^{*\pm}(1385)$, respectively [15]. In 147 GeV/c π^+p interactions, inclusive $\Sigma^{*+}(1385)$ was observed with a cross section of 290±70 μb, and an upper limit was set on $\Sigma^{*-}(1385)$ production of 100 μb [17]. At the ISR $\Sigma^{*\pm}(1385)$ and $\Xi^-(1320)$ were observed for $X_F > 0.4$ with cross sections 250 μb, 40 μb, and 9 μb for Σ^{*+}, Σ^{*-} and Ξ^- respectively [24]. The latter experiment has studied the proton fragmentation region, while this experiment observes the forward hemisphere consisting of the central and π^- fragmentation regions.

Our results show that the $K^{*\pm}$ cross sections increase with beam energy and that these are consistent with other data. The Ξ^- cross section is consistent with low energy result assuming the logarithmic energy dependence of cross sections. In case of $\Sigma^{*\pm}$, the low energy π^- data show an increase of the cross sections with beam energy. Assuming similar trends to the π^- and proton data, we expect the cross sections for the $\Sigma\alpha^{*\pm}$ production to be at least ~300 μb at 200 GeV/c. This suggests that our cross sections may be underestimated, or that the energy dependence is weaker than for other beams.

4.1 Observation of Λ_c^+: The invariant mass distribution for $K_S^o p^{\pm}\pi^+\pi^-$, which may reveal the Cabibbo allowed decay channel of Λ_c, is seen in Fig. 4.1.1. A narrow peak consistent with our mass resolution of 13.5 ± 5.9 MeV/c² at ~ 2.300 GeV/c² is close to the world average mass Λ_c^+[13]. We do not observe a similar peak in the $K_S^o p\pi^{\pm}\pi^{\pm}$ and $K_S^o \bar{p}\pi^{\pm}\pi^{\pm}$ distributions. The individual $K_S^o p^{\pm}\pi^+\pi^-$ invariant mass distributions together with their sum are seen in Fig. 4.1.2. In Fig. 4.1.3 we fit the combined distribution in 20 MeV/c² bins to a Gaussian with width equal to our resolution and a $[A(M-m_o) + B(M-m_o)^2 + C(M-m_o)^3]\exp[-D(M-m_o)]$ background. The fitted mass is 2311±5 MeV/c² with 41±12 events (χ^2/DOF = 31.59/44).

To check if the signal is caused by the Cherenkov threshold defining the proton or particle misidentification, we plot the invariant mass distributions with proton momentum in range 23.5-38.8 GeV/c and 25-38.8 GeV/c, as seen in Fig. 4.1.4, without diminishing the significance of the peak. In Fig. 4.1.5, we plot the K_S^o"$p^{\pm}$"$\pi^+\pi^-$ effective mass distributions with particles having momentum between 20-38.8 GeV/c and produced light defined as protons. We do not observe a peak at ~2.3 GeV/c². The observed narrow peak ~2.2 GeV/c² is due to the Cherenkov threshold, since plotting the same mass distributions with proton momentum between 23.5-38.8 GeV/c the peak disappears. To further study the particle misidentification, we plot the invariant mass distribution K_S^o"$K^{\pm}$"$\pi^+\pi^-$ and K_S^o"$\pi^{\pm}$"$\pi^+\pi^-$, where "$K^{\pm}$" and "$\pi^{\pm}$" are

particles with momentum between 20-38.8 GeV/c, no light and defined as kaon and pion, respectively, as seen in Fig. 4.1.6. In effect we replace the protons with kaons or pions. Shaded histograms are the events from mass band 2.29-2.33 GeV/c² in the mass distributions $K_S^o p^{\pm}\pi^+\pi^-$ when protons are replaced by kaons or pions. From these plots we conclude that the signal in the $K_S^o p^{\pm}\pi^+\pi^-$ mass distributions is not connected with the reflection of known resonances. Also, it is difficult to associate the observed signal with baryon resonances because the typical width of these, in this mass range, is 100-200 MeV/c². Based on the width of the peak the most plausible explanation is the charmed baryon Λ_c^+, however our observed mass is ~30 MeV/c² higher than the currently accepted value of 2282.0±3.1 MeV/c² [13].

The X_F and P_T^2 distributions for this peak, seen in Fig. 4.1.7, were parameterized as $(1-X_F)^n$ and $\exp(-bP_T^2)$, respectively. The fit gives $n = 2.82\pm2.20$ (χ^2/DOF = 2.46/3) for $0.2 \leq X_F < 0.7$ and $b = 2.15\pm0.89$ $(\mathrm{GeV/c})^{-2}$ (χ^2/DOF = 1.24/3).

4.2 <u>Cross Section</u>: The geometrical and decay volume efficiency for this peak at 2.3 GeV/c², 0.04, is essentially determined by the requirement that the proton momentum be between 20.0 and 38.8 GeV/c. To obtain this efficiency we use Monte-Carlo generated events of Λ_c^+ decaying into $K_S^o p\pi^+\pi^-$ with P_T^2 distributed as $\exp(-1.1P_T^2)$ and a flat X_F distribution. Also a $(1-X_F)^2$ distribution was tried and the results were consistent. It was found that only Λ_c with $0.1 \leq X_F < 0.7$ can be

detected by the apparatus. The trigger efficiency is 0.12 for the events with the number of charged tracks ≥ 3. Using 41±12 observed events of $\Lambda_c/\bar{\Lambda}_c$ and assuming a linear A dependence we obtain the cross section times the branching fraction $\sigma \cdot BR = 1.90 \pm 0.86$ μb/nucleon for the $\bar{K}^o p\pi^+\pi^-/K^o\bar{p}\pi^+\pi^-$ decay mode. Branching fractions for this decay mode are not well known. The Particle Data Group quotes only the upper limit of 4% [13]. Recently, the BIS-2 Collaboration observed the Λ_c^+ production by neutrons on carbon and hydrogen at 40-70 GeV. They measured the relative branching ratio of $\sigma \cdot BR(\bar{K}^o p\pi^+\pi^-)/\sigma \cdot BR(\Lambda\pi^+\pi^+\pi^-) = 4.3 \pm 1.2$ [26]. Using this result and assuming a branching fraction of 3.1% for the $\Lambda^o\pi^+\pi^+\pi^-$ decay mode we obtain a cross section 14.3±7.6 μb/nucleon for the production $\Lambda_c/\bar{\Lambda}_c$. This cross section is much higher than expected relative to the cross sections for the production of other states (Table 3.4.1). Also, the obtained cross section is not consistent with other data on charm production in hadron interactions. In 360 GeV/c π^-p interactions, the LEBC-EMS Collaboration estimates an upper limit for the cross section $\sigma(\Lambda_c) \leq 4$ μb ($X_F>0$) and a preliminary estimate for the inclusive total charm cross section in the forward hemisphere 17 μb $\leq \sigma(\text{charm}) \leq$ 22 μb [25]. In pp interactions at the same energy they estimate the $D\bar{D}$ and $\Lambda_c\bar{D}$ pair cross sections for all X_F: $\sigma(D\bar{D}) = 19^{+13}_{-5}$ μb and $\sigma(\Lambda_c\bar{D}) = 18^{+15}_{-10}$ μb [27]. An emulsion experiment with protons at 400 GeV obtains the inclusive Λ_c^+ cross section of 62±27 μb/nucleon [28]; and the ACCMOR Collaboration estimates the upper limit for production Λ_c^+, $\sigma(\Lambda_c^+) \leq 8$ μb/nucleon, in 150 GeV/c pBe interactions. The observation of Λ_c^+ with neutrons at 40-70 GeV/c on a

carbon target is reported by BIS-Collaboration yielding $\sigma(\Lambda_c^+) \geq 13.4$ μb/nucleon [26]. Our high Λ_c cross section can indicate that we do not understand completely the whole acceptance corrections for the production of this specific state; or that some narrow width non-charm hyperon at ~2300 MeV/c² has been observed in this experiment.

If this peak is the Λ_c, it is one of the first evidence for its production by pions. The LEBC-EHS collaboration reports 4 events (decaying into $\Sigma^+\pi^+\pi^-$, $\bar{\Lambda}^\circ\pi^+\pi^-\pi^-$, $K^+\bar{p}\pi^-$, and $K^-p\pi^+$) produced in 360 GeV/c π^-p interaction [25].

CONCLUSIONS

In the presented analysis, we studied the strange resonance production in $\pi^- N$ interactions at 200 GeV/c with only one K^o_S, Λ or $\bar{\Lambda}$ in the final state. For each state we presented X_F and P_T^2 distribution with the parameterization $(1-X_F)^n$ and $\exp(-bP_T^2)$ respectively. We compare the fitted exponent n with the QCD quark counting rules predictions. Also, we calculated the cross sections for each state. Where it was possible, we compared our results with those from other experiments.

In the $K^*(892)$ production, we observed no difference between our charged (K^{*-}, K^{*+}) and the neutral $(K^{*o}, \bar{K}^{*o})$ components from other experiment, but the individual values of n are all systematically lower than QCD quark counting rule predictions. About one third of the K^o_S came from K^* decay.

In strange baryon productions we observe that the value n is consistent with the quark counting rules within the limits of the errors. These results demonstrate the significant role of valence quarks in strange resonance production. The QCD quark counting rules gave a rough estimate and a convenient parameterization of the X_F spectra, but these results and other data indicate systematic differences, probably related to spin and flavor effects. Under reasonable assumptions, we gave the cross section for the diffractive dissociation process $\pi^- \to K^o K^- \pi^+ \pi^-$ and $\bar{K}^o K^+ \pi^- \pi^-$ which is consistant with the expected estimate.

Finally, we observe a narrow state, consistent with our mass resolution, decaying into $K^o_S p^{\pm}\pi^+\pi^-$ at a mass 2311±5 MeV/c² with n = 2.82±2.20 and b = 2.15±0.89(GeV/c)$^{-2}$. Our interpretation of this state is the $\Lambda^+_c(2282)$, but two pieces of evidence dilute this interpretation: the observed mass is ~30 MeV/c² higher than the currently accepted mass and the cross section is too large with respect to observed strange resonance cross sections and to other charm hadron production data.

Appendix A: Diffractive Production

Although diffractive dissociation has been widely observed in high energy hadro-production experiments, relatively little information is a available on the flavor dependence of this process [29]. Recently, the experiment E580 has reported the study of the diffractive fragmentation of a π^- beam into $K^o_S K^o_S \pi^-$ and $K^o_S K^o_S \pi^+ \pi^- \pi^-$ [15]. The ratio of the $K^o_S K^o_S \pi^+ \pi^- \pi^-$ cross section (1.59±0.78 μb) to the diffractive $K^o_S K^o_S \pi^-$ cross section (3.4±1.1 μb) is 0.40±0.13, in good agreement with the value 0.36 expected in the diffractive fragmentation picture assuming for the asymptotic topological cross section $\sigma = C/NTOT^2$, where C is a constant and NTOT is the multiplicity for charged plus neutral particles.

From the above results, we expect the cross section for the diffractive dissociation process $\pi^- \to K^o K^- \pi^+ \pi^-$ or $\pi^- \to \bar{K}^o K^+ \pi^- \pi^-$ will be at the level ~ 8-10 μb. To test this hypothesis we chose the reaction $\pi^- \to K^o_S \pi^+ \pi^- \pi^-$, assuming that one pion is the unidentified kaon to compensate the strangeness. This analysis is based on a sample of 4,255 K^o_S events with one positive primary track and two negative primary tracks passing through the spectrometer. To isolate the diffractive component in our $K^o_S \pi^+ \pi^- \pi^-$ data, we plot the recoiling mass squared (MM^2) as the unshaded histogram of Fig. A.1a, assuming a nucleon target. The low mass peak centered at $1(GeV/c^2)^2$ is interpreted as the recoiling nucleon system.

In the analysis of exclusive reactions considerable effort is made to eliminate or correct for the non-diffractive background. The shaded

histogram in Fig. A.1a shows the recoiling mass squared distribution of the $K_S^o\pi^+\pi^+\pi^-$ system. As expected, we do not see the low mass peak in this figure since the net positive charge of this final state could not be produced diffractively. Since this state has the same number of particles as the $K_S^o\pi^+\pi^-\pi^-$ state, we use this data as an estimate of the non-diffractive background in the $K_S^o\pi^+\pi^-\pi^-$ channel. Fitting a polynomial distribution to the shaded histogram and normalizing the resulting fit to the unshaded histogram of Fig. A.1a between $203.5(GeV/c^2)^2$ and $273.5(GeV/c^2)^2$, we obtain the solid curve shown in the figure; subtracting, we obtain Fig. A.1b. To correct for the diffractive events with an unseen π^o, we assume the effect on the MM^2 distribution caused by removing a π^o from $K_S^o\pi^+\pi^-\pi^-\pi^o$ is similar to removing the π^+ from $K_S^o\pi^+\pi^-\pi^-$. We therefore use the $K_S^o\pi^+\pi^-\pi^-$ events with $MM^2 < 18.5(GeV/c^2)^2$, throw out the only π^+, recalculate the missing mass squared of the remaining $K_S^o\pi^-\pi^-$ and plot it in Fig. A.1c. Normalizing the histogram in Fig. A.1c between 23.5 and $273.5(GeV/c^2)^2$ to the histogram in Fig. A.1b and then subtracting, we obtain the result shown in Fig. A.1d. A prominent low mass peak results whose FWHM is consistent with the calculated spectrometer MM^2 resolution of $14(GeV/c^2)^2$(FWHM). In the figure there are 304±30 events with $MM^2 < 18.5(GeV/c^2)^2$ which are assumed to be primarily single diffractive events plus some double diffractive events. To check this result, we fit the logarithmic-normal distribution, plus polynomial background to the MM^2 distribution for $K_S^o\pi^+\pi^-\pi^-$ events, Fig. A.1e. In Fig. A.1f we plot the fitted logarithmic-normal distribution (solid curve) [30] with

the MM^2 distribution after the background subtraction. We obtain 300^{+38}_{-22} $K^o_S\pi^+\pi^-\pi^-$ diffractive events with $MM^2 < 18.5(GeV/c^2)^2$, which is in excellent agreement with 304±30 events obtained by the first method.

To obtain the cross section we normalize our K^o_S sample to the bubble chamber cross section for the inclusive, single K^o_S production in a forward direction, 1.41±0.28mb [22]. Comparing the geometrical decay volume acceptances and trigger efficiencies for diffractive events and all K^o_S events, we obtain the cross section for the single diffractive $\pi^-\to K^oK^-\pi^+\pi^-$ and $\bar{K}^oK^+\pi^-\pi^-$, 11.18±5.91 μb per channel, assuming that both diffractive channels contribute equally. This cross section is in good agreement with the expected value.

REFERENCES

1. F. Halzen and A.D. Martin, Quark and Leptons: An Introductory Course in Modern Particle Physics, (Wiley, New York, 1984); and K. Huang, Quarks, Leptons and Gauge Fields,(World Scientific, Singapore, 1982).

2. M. Gell-Man, Phys. Lett. 8, 214 (1964); and G. Zweig, CERN preprint Rep. TH 401 (unpublished) (1964).

3. R.P. Feynman, Photon-Hadron Interactions, (Benjamin, New York, 1972).

4. P.D.B. Collins and A.D. Martin, Rep. Prog. Phys. 45, 335 (1983); and K. Fialkowski and W. Kittel, Rep. Prog. Phys. 46, 1283 (1983).

5. J.F. Gunion, Phys. Lett. B88, 150 (1979).

6. J.D. Bjorken and S.L. Glashow, Phys. Lett. 11, 255 (1964).

7. S.L. Glashow, J. Iliopoulos and L. Maiani, Phys. Rev. D2, 1285 (1970).

8. J.J. Aubert, et al., Phys. Rev. Lett. 33, 1404 (1974); and J.E. Augustin, et al., Phys. Rev. Lett. 33, 1406 (1974).

9. G. Goldhaber, et al., Phys. Rev. Lett. 37, 255 (1976); and I. Peruzzi, et al., Phys. Rev. Lett. 37, 569 (1976).

10. M.K. Gaillard, B.W. Lee and J.L. Rosner, Rev. Mod. Phys. 47, 277 (1975); and A. de Rujula, H. Georgi and S.L. Glashow, Phys. Rev. D12, 147 (1975).

11. E. Leader and E. Predazzi, An Introduction to Gauge Theories and the New Physics, (Cambridge Press, New York, 1983).

12. G.H. Trilling, Phys. Rep., 75, 59 (1981).

13. C.G. Wohl, et al., [Particle Data Group], Rev. Mod. Phys. 56, S1 (1984).

14. A. Kernan and G. VanDalen, Phys. Rep. 106, 298 (1984).

15. T.Y. Chen, et al., Phys. Rev. D28, 2304 (1983); C.C. Chang, et al., Phys. Rev. D29, 1888 (1984); H.C. Fenker, et al., Phys. Rev. D30, 872 (1984); E.G.H. Williams, et al., Phys. Rev. D30, 877 (1984); and A. Napier, et al., Phys. Lett. B149, 514 (1984).

16. S. Torres, PhD Thesis, VPI, 1984.

17. D. Brick, et al., Phys. Rev. D25, 2248 (1982).

18. R. Bailey, et al., Z. Phys. 24, 111 (1984).

19. A.E. Brenner, et al., Phys. Rev. D26, 1497 (1982).

20. R.T. Edwards, et al., Phys. Rev. D18, 76 (1978).

21. D. Cutts, et al., Phys. Rev. Lett. 43, 319 (1979).

22. D. Bogert, et al., Phys. Rev. D16, 2098 (1977).

23. N.N. Biswas, et al., Nucl. Phys. B167, 41 (1980).

24. S. Erhan, et al., Phys. Lett. B85, 447 (1979).

25. J. Hrubec, in XII International Conference on High Energy Physics, edited by A. Meyer and E. Wieczorek (Akademie der Wissenschaften der DDR, Berlin-Zeuthen, 1984).

26. H. Nowak, in XII International Conference on High Energy Physics, edited by A. Meyer and E. Wieczorek (Akademie der Wissenschaften der DDR, Berlin-Zeuthen, 1984).

27. M. Aguilar-Benitez, et al., Phys. Lett. B123, 103 (1983).

28. A. Gurtu, in Multiparticle Dynamics 1984, edited by G. Gustafson and C. Petersen (World Scientific, Singapore, 1984) pp.264-281.

29. G. Alberi and G. Goggi, Phys.Rep. 74, 2 (1981); K. Goulianos, Phys.Rep. 101, 174 (1983).

30. W.T. Eadie, et al., Statistical Methods in Experimental Physics, (North-Holland, Amsterdam, 1973).

Table 1.1. Spin 0 charm mesons and spin $\frac{1}{2}$ charm baryons.

Name	Quarks	$SU_c(3)$	Isospin (I, I_3)	Strangeness (s)	Charm (c)
MESONS					
D^+	$c\bar{d}$	$\bar{3}$	$\frac{1}{2}, \frac{1}{2}$	0	+1
D°	$c\bar{u}$	$\bar{3}$	$\frac{1}{2}, -\frac{1}{2}$	0	+1
F^+	$c\bar{s}$	$\bar{3}$	0, 0	+1	+1
$\bar{D}^\circ$	$\bar{c}u$	3	$\frac{1}{2}, \frac{1}{2}$	0	-1
D^-	$\bar{c}d$	3	$\frac{1}{2}, -\frac{1}{2}$	0	-1
F^-	$\bar{c}s$	3	0, 0	-1	-1
η_c	$c\bar{c}$	1	0, 0	0	0
BARYONS					
Σ_c^{++}	cuu	6	1, 1	0	1
Σ_c^+	c(ud)	6	1, 0	0	1
Σ_c°	cdd	6	1, -1	0	1
S^+	c(us)	6	$\frac{1}{2}, \frac{1}{2}$	-1	1
S°	c(ds)	6	$\frac{1}{2}, -\frac{1}{2}$	-1	1
T°	css	6	0, 0	-2	1
Λ_c^+	c(ud)	$\bar{3}$	0, 0	0	1
A^+	c(us)	$\bar{3}$	$\frac{1}{2}, \frac{1}{2}$	-1	1
A°	c(ds)	$\bar{3}$	$\frac{1}{2}, -\frac{1}{2}$	-1	1
X_u^{++}	ccu	3	$\frac{1}{2}, \frac{1}{2}$	0	2
X_d^+	ccd	3	$\frac{1}{2}, -\alpha_2$	0	2
X_s^+	ccs	3	0, 0	-1	2

Table 1.2. Selection rules for charm quark decay. [12]

Selection rules		
Dependence	c decay	$\bar{c}$ decay
Leptonic or semileptonic modes		
$\cos\theta_c$	$\Delta S = \Delta C = \Delta Q = -1$	$\Delta S = \Delta C = \Delta Q = +1$
	$\Delta I_3 = \lvert\Delta I\rvert = 0$	$\Delta I_3 = \lvert\Delta I\rvert = 0$
$\sin\theta_c$	$\Delta C = \Delta Q = -1$	$\Delta C = \Delta Q = +1$
	$\Delta S = 0$	$\Delta S = 0$
	$\Delta I_3 = -\frac{1}{2}$, $\lvert\Delta I\rvert = \frac{1}{2}$	$\Delta I_3 = +\frac{1}{2}$, $\lvert\Delta I\rvert = \frac{1}{2}$
Hadronic modes		
$\cos^2\theta_c$	$\Delta S = \Delta C = -1$	$\Delta S = \Delta C = +1$
	$\Delta I_3 = +1$, $\lvert\Delta I\rvert = 1$	$\Delta I_3 = -1$, $\lvert\Delta I\rvert = 1$
$\cos\theta_c\sin\theta_c$	$\Delta S = 0$, $\Delta C = -1$	$\Delta S = 0$, $\Delta C = +1$
	$\Delta I_3 = +\frac{1}{2}$, $\lvert\Delta I\rvert = \frac{1}{2}, \frac{3}{2}$	$\Delta I_3 = -\frac{1}{2}$, $\lvert\Delta I\rvert = \frac{1}{2}, \frac{3}{2}$
$\sin^2\theta_c$	$\Delta S = +1$, $\Delta C = -1$	$\Delta S = -1$, $\Delta C = +1$
	$\Delta I_3 = 0$, $\lvert\Delta I\rvert = 0, 1$	$\Delta I_3 = 0$, $\lvert\Delta I\rvert = 0, 1$

Table 2.1.1. Cherenkov C_B physical characteristics.

Dimensions	226 × 122 × 330 cm^3
Mirror area	322 × 142 cm^2
Gas	N_2
Refractive index	1.0003
Radiator length	177 cm
Cone radius (β = 1)	4 cm
Mirrors	30
Mirror to target	8.7 m
Pion threshold	5.7 GeV/c
Kaon threshold	20.0 GeV/c
Proton threshold	38.8 GeV/c

Table 3.3.1. Fits to X_F distribution of the form $(1-X_F)^n$.

Reaction	X_F range	n	χ^2/DOF	QCR n [5]
$\pi^-(\bar{u}d) \to K^\circ_S$	0.2-0.8	1.66±0.05	9.51/13	1,3
$\to K^{*-}(\bar{u}s)$	0.2-1.0	0.86±0.20	2.59/2	1
$\to K^{*+}(u\bar{s})$	0.2-1.0	1.86±0.36	1.09/2	3
$\to \Lambda(uds)$	0.2-0.8	1.97±0.11	6.83/11	2
$\to \bar{\Lambda}(\bar{u}\bar{d}\bar{s})$	0.2-0.8	1.96±0.13	11.54/11	2
$\to \Sigma^{*-}(dds)$	0.0-1.0	1.44±0.41	0.004/3	2
$\to \Sigma^{*+}(uus)$	0.0-0.8	3.81±2.16	0.07/2	4
$\to \Xi^-(dss)$	0.0-1.0	2.21±1.95	1.11/2	2
$\to \bar{\Xi}^+(\bar{d}\bar{s}\bar{s})$	0.0-1.0	8.40±9.09	1.13/2	4

Table 3.4.1 The cross sections for observed states.

States	Observed No. of events	Partial Cross-Section † [μb]	Total Cross-Section †† [μb]
K°_{S}	25,565	109.14±45.00	-
Λ	3,999	22.59±9.32	-
$\bar{\Lambda}$	3,041	17.18±7.08	-
$K^{*-}(892)$	2,706±313	32.20±13.79	1,103.54±168.81
$K^{*+}(892)$	1,813±309	21.58±9.62	739.36±146.01
$\Sigma^{-}(1385)$	219±50	1.55±0.73	105.16±30.13
$\Sigma^{+}(1385)$	154±46	1.09±0.57	73.95±25.53
$\Xi^{-}(1321)$	48±10	0.52±0.24	35.06±9.50
$\Xi^{+}(1321)$	33±10	0.36±0.18	8.91±2.98

† based on forward sensitivity $S=(N_t N_b)^{-1}=(328.27*10^2 \text{events}/\mu b)^{-1}$ with associated low charged multiplicity.

†† based on average normalization to the bubble chamber data [23].

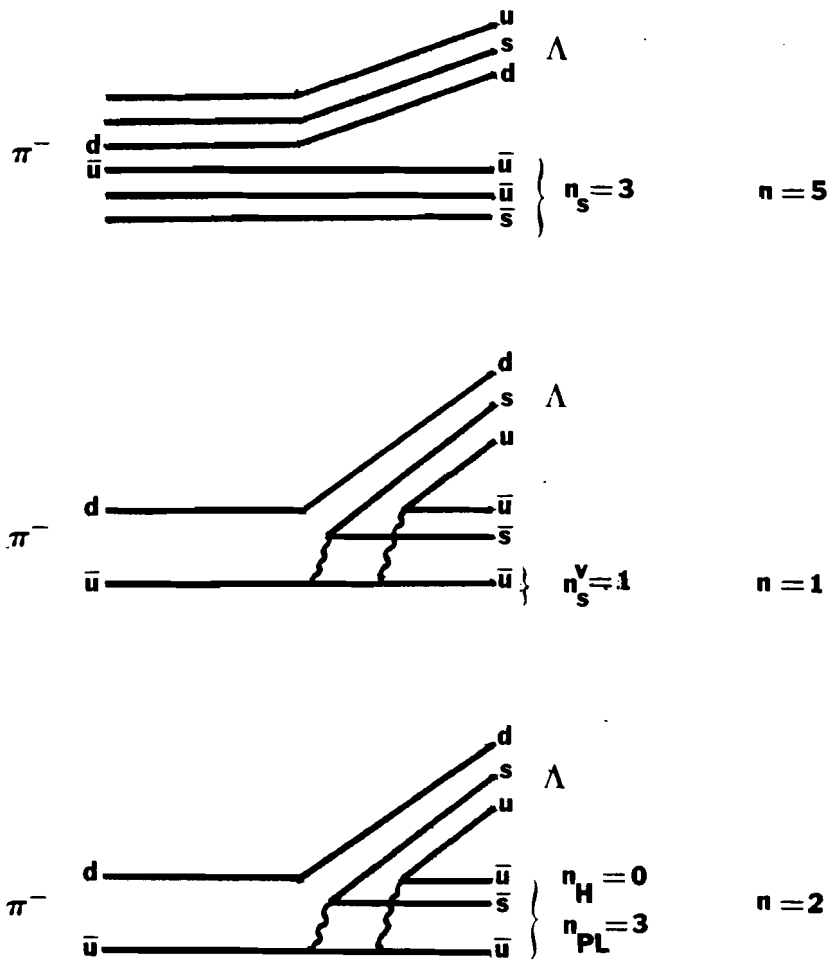

Fig. 1.1: Fragmentation diagrams for $\pi^- \to \Lambda$.

E580 LAYOUT

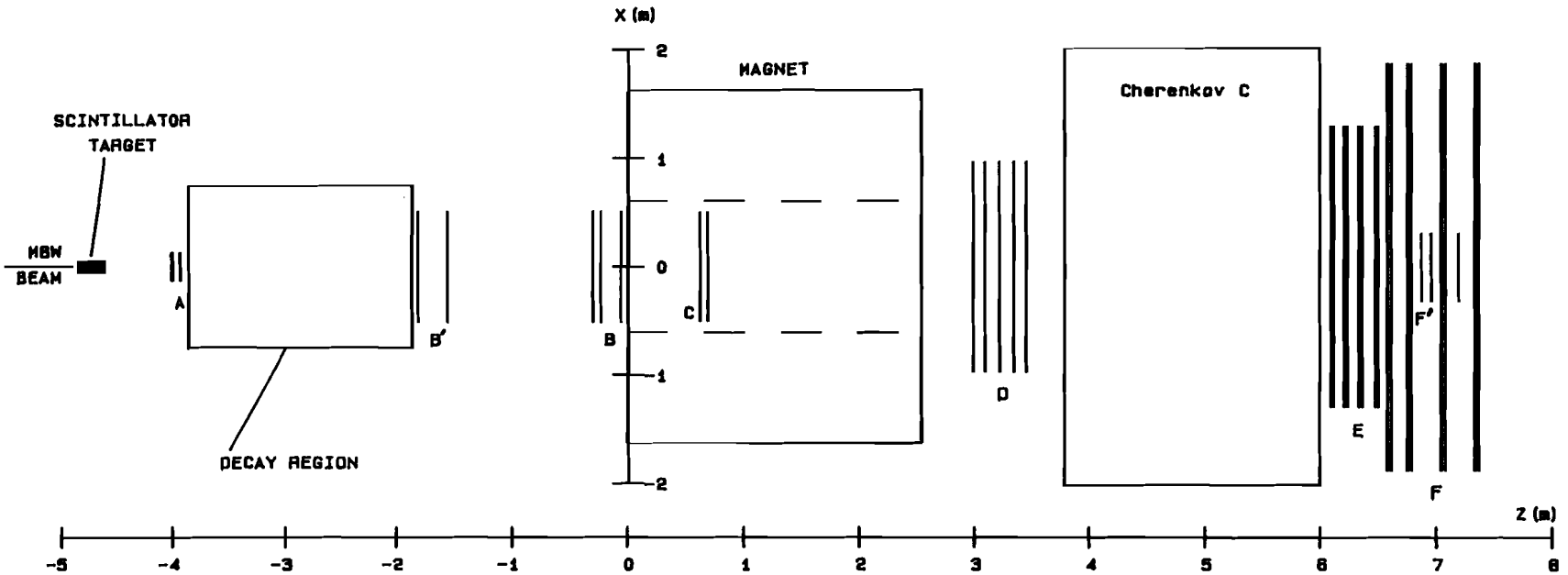

BEAM CHAMBERS

PWCs	Spacing	Planes
BA1	2 mm	Y X
BA2	2 mm	Y X U
BB	1 mm	Y U X

CHAMBER PARAMETERS

PWCs	Spacing	Planes	Wires
A	1 mm	X X1 Y Y1 U V	1536
B' B	2 mm	X X1 X Y X1	2112
C	2 mm	X Y	832
D	2 mm	X U Y V X1	3968
F'	2 mm	X Y V	960

Spark Chambers

E	4 modules	(X Y U)
F	4 modules	(X Y U)

Fig. 2.1.1: Plan view of experimental apparatus.

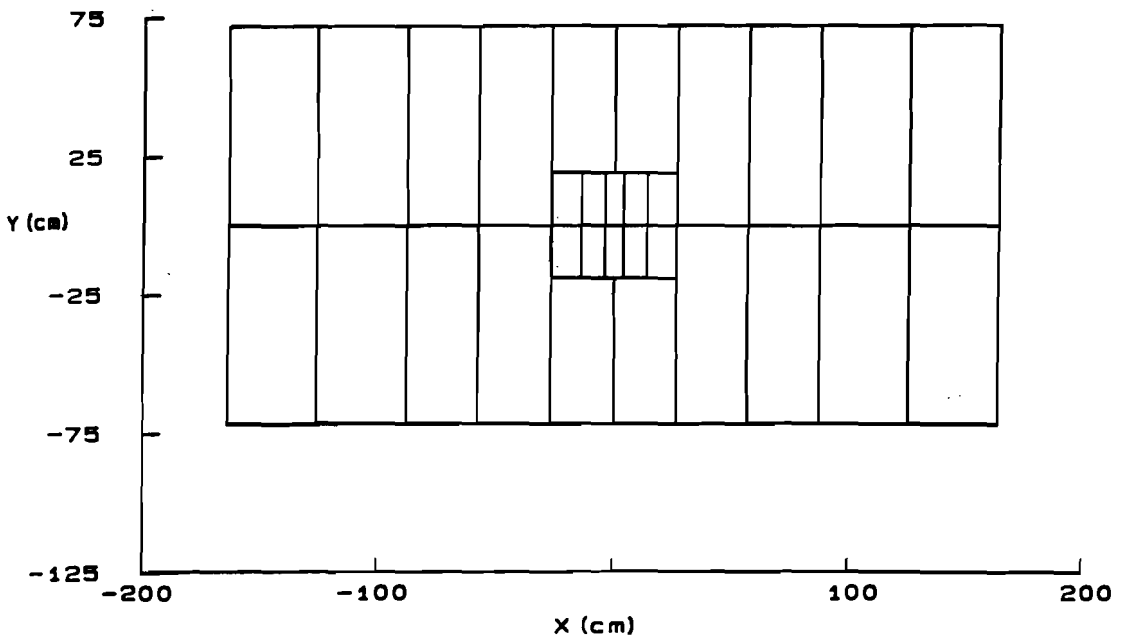

Fig. 2.1.2: Cherenkov mirror plane segmentation.

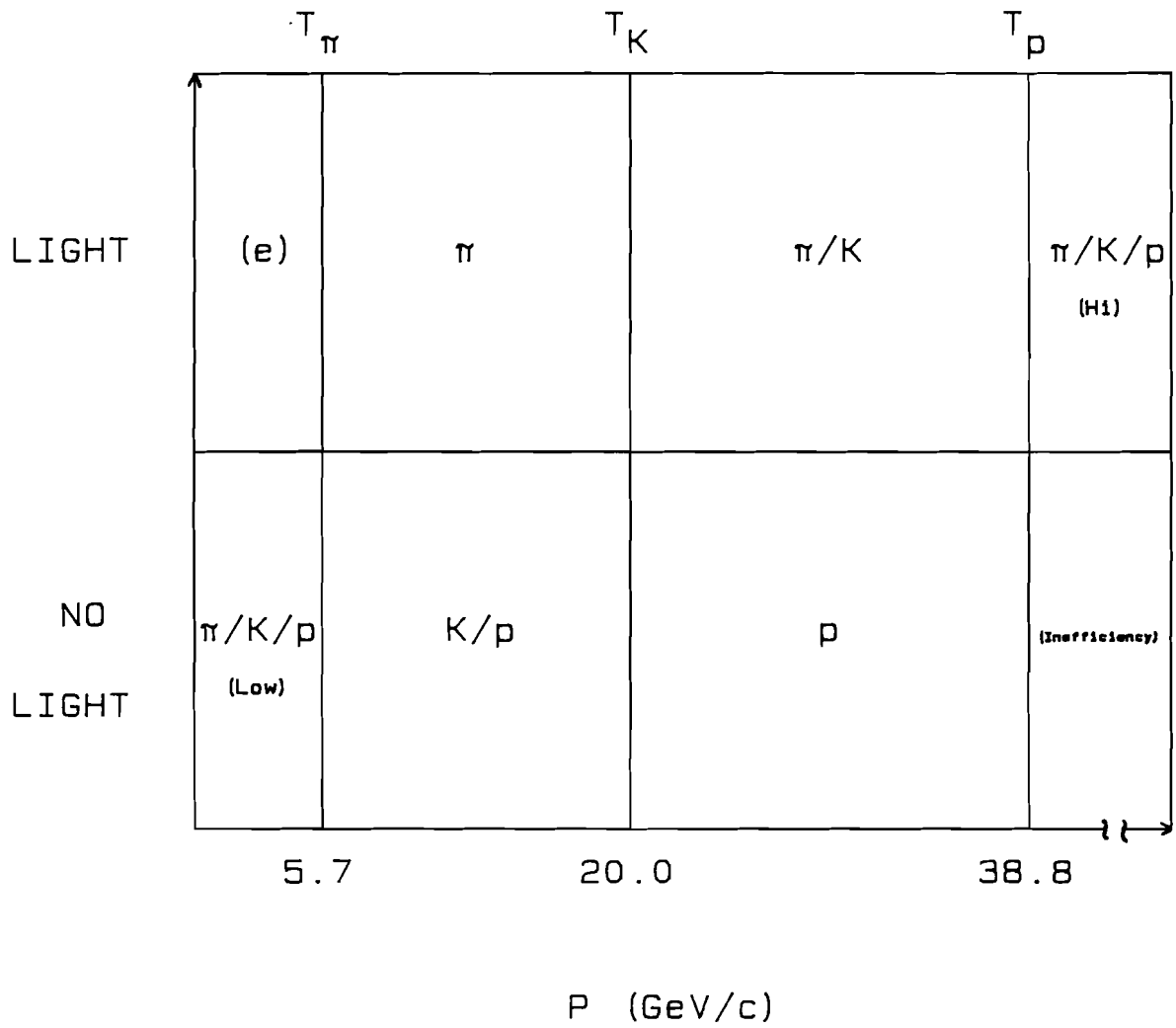

Fig. 2.4.1: Particle identification momenta regions.

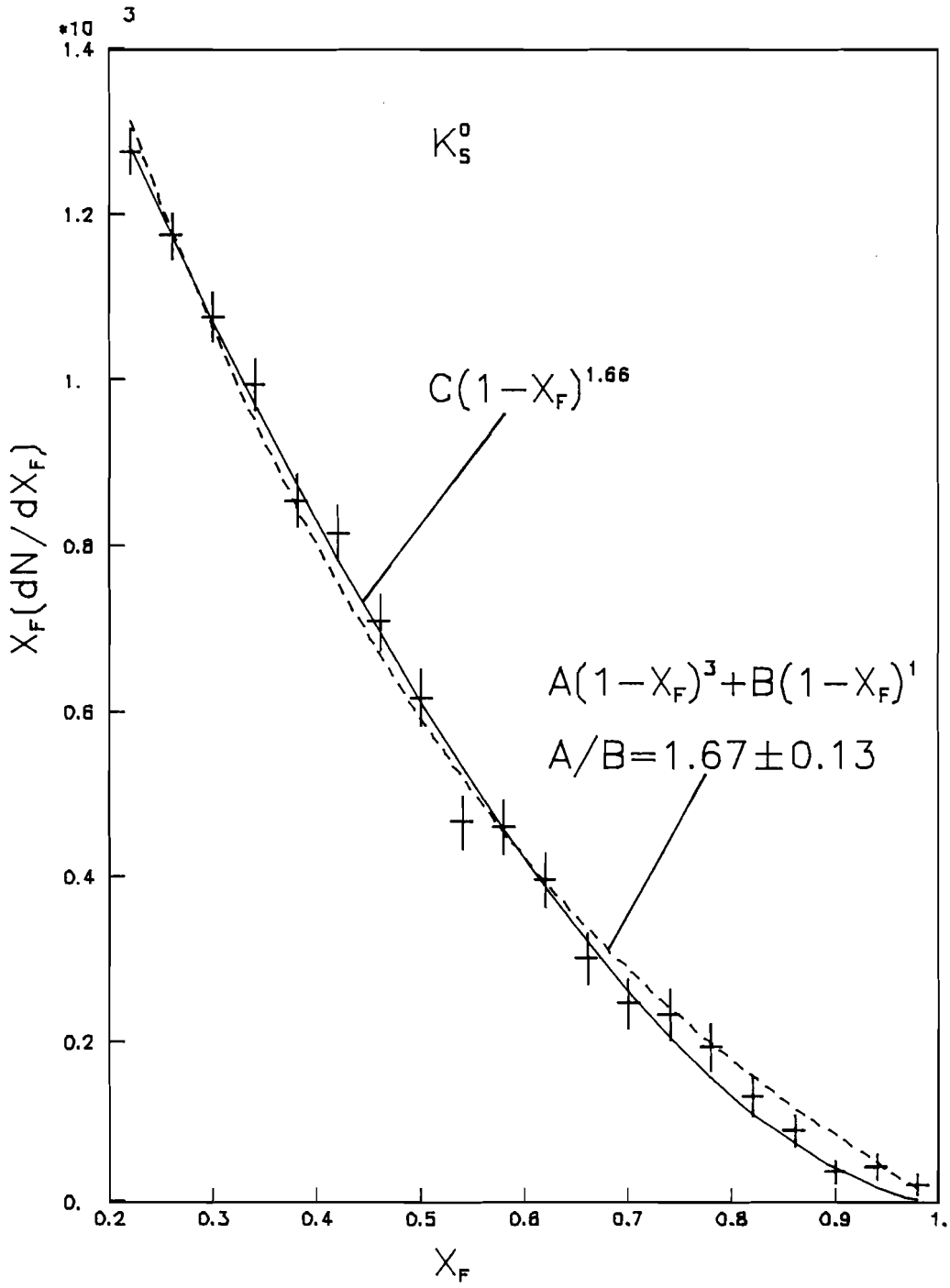

Fig. 3.1.1: The K_S^o invariant X_F distribution.

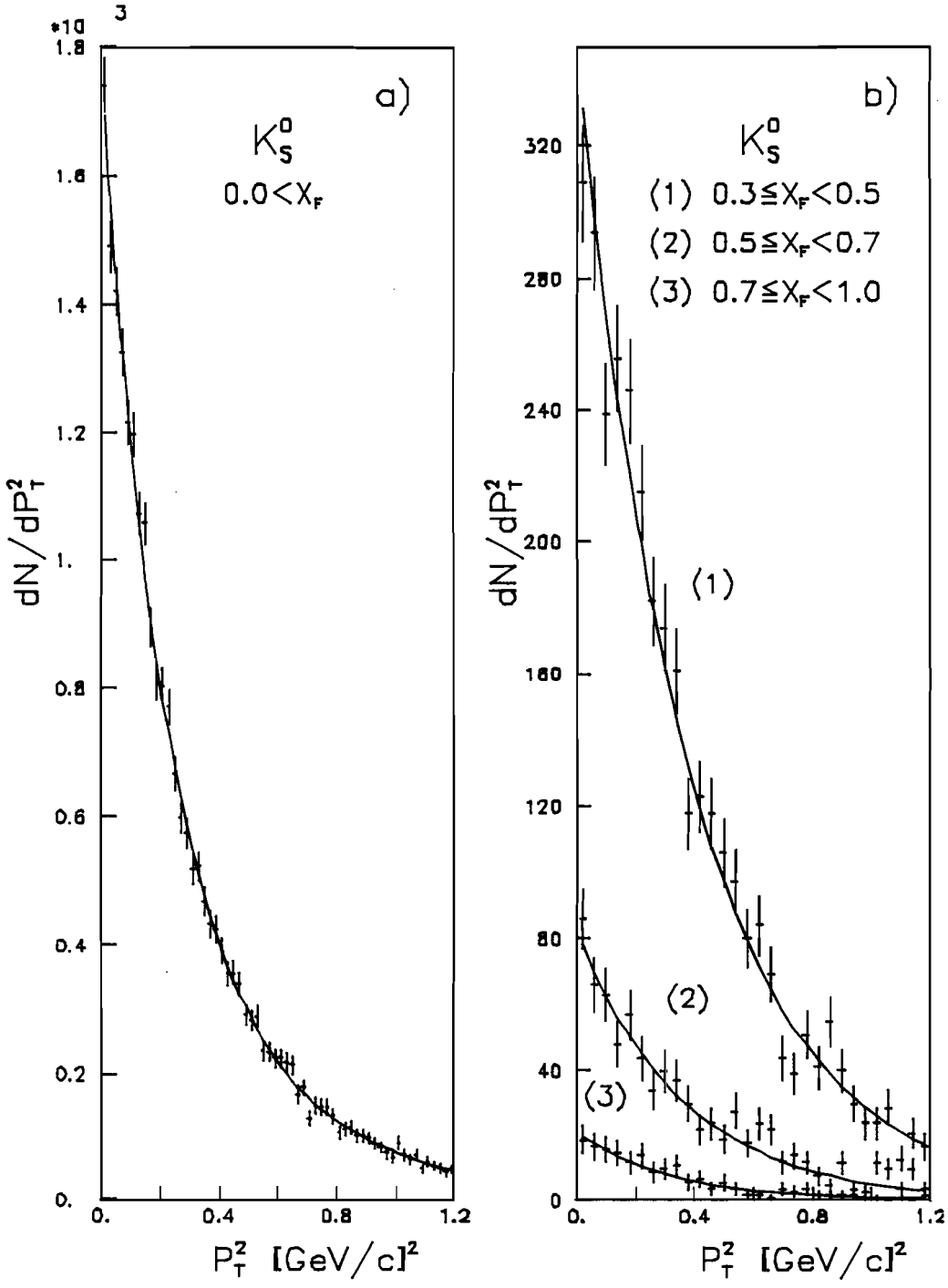

Fig. 3.1.2: The K_S^0 P_T^2 distribution for (a) $X_F > 0.0$ and (b) $0.3 \leq X_F < 0.5$, $0.5 \leq X_F < 0.7$, $0.7 \leq X_F < 1.0$.

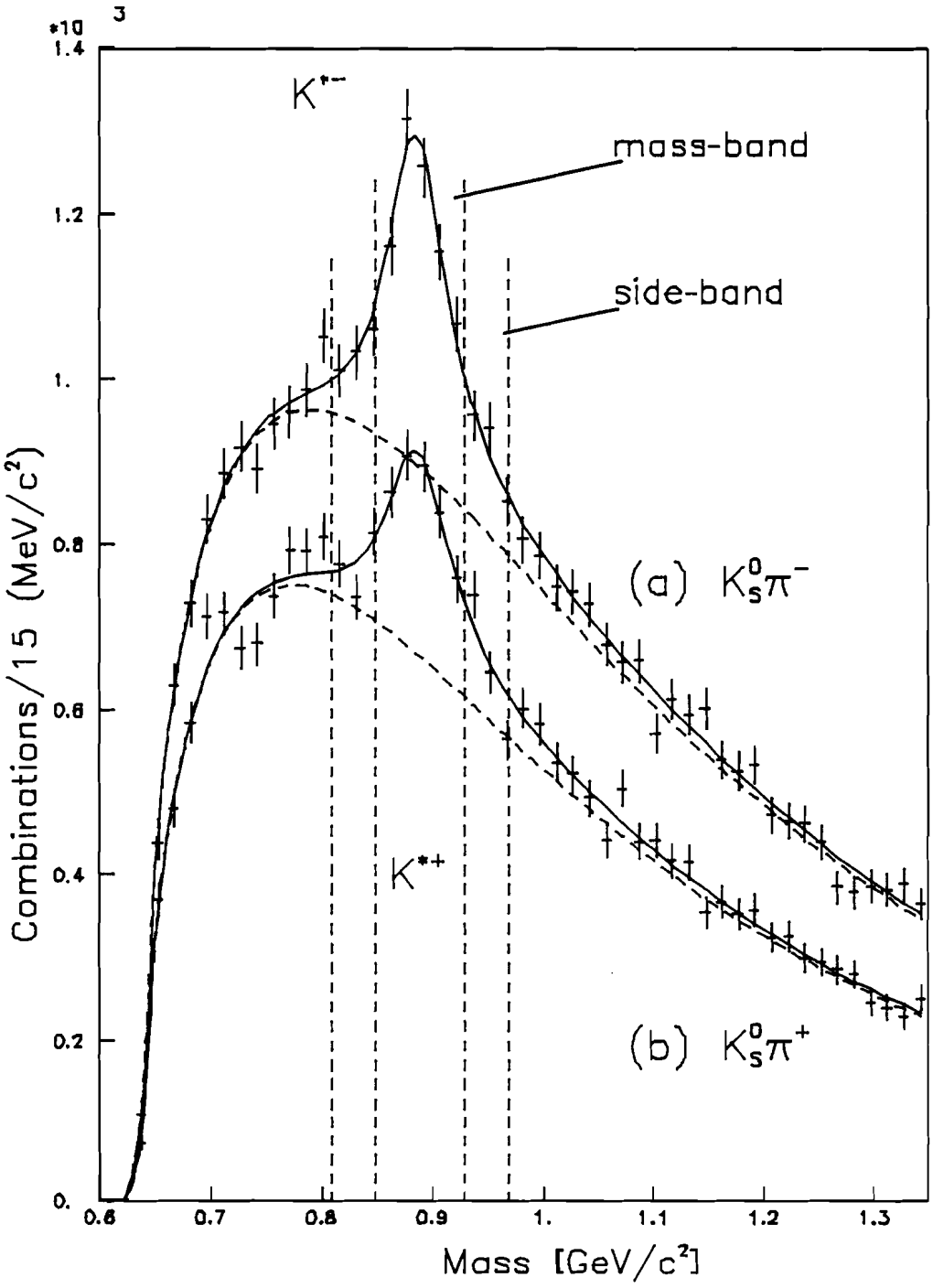

Fig. 3.1.3: Mass spectra for $K_S^o\pi^-$ and $K_S^o\pi^+$.

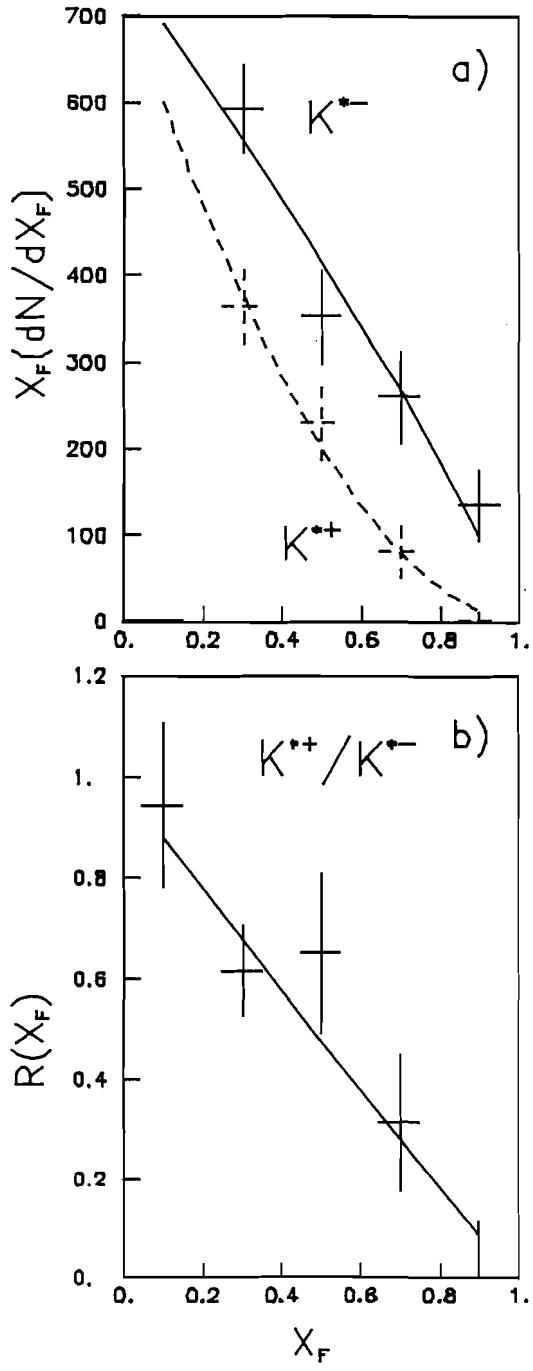

Fig. 3.1.4: The invariant X_F distributions for (a) K^{*-} and K^{*+} (b) the K^{*+} to K^{*-} ratio.

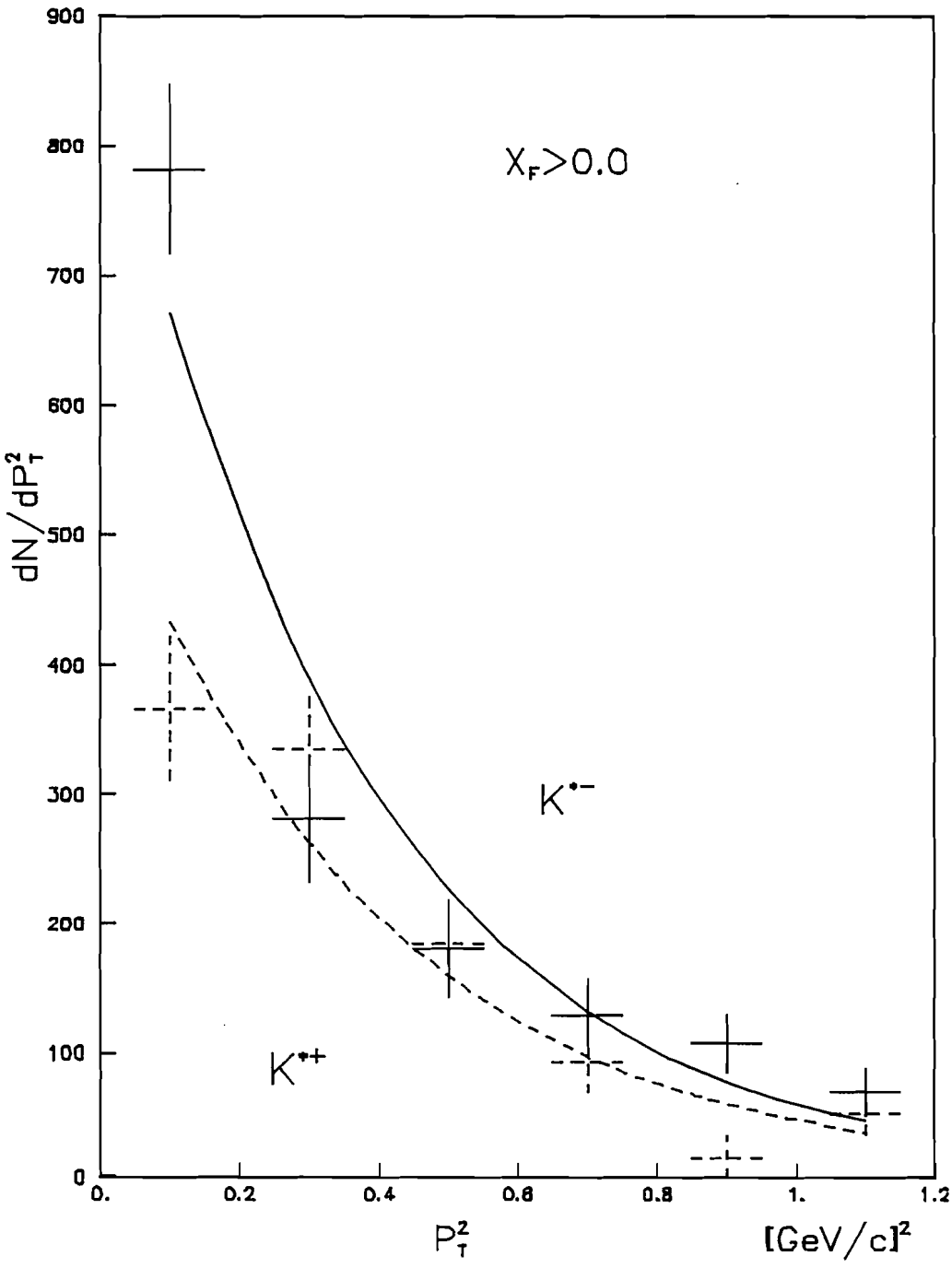

Fig. 3.1.5: The P_T^2 distribution for $X_F>0.0$ for K^{*-} and K^{*+}.

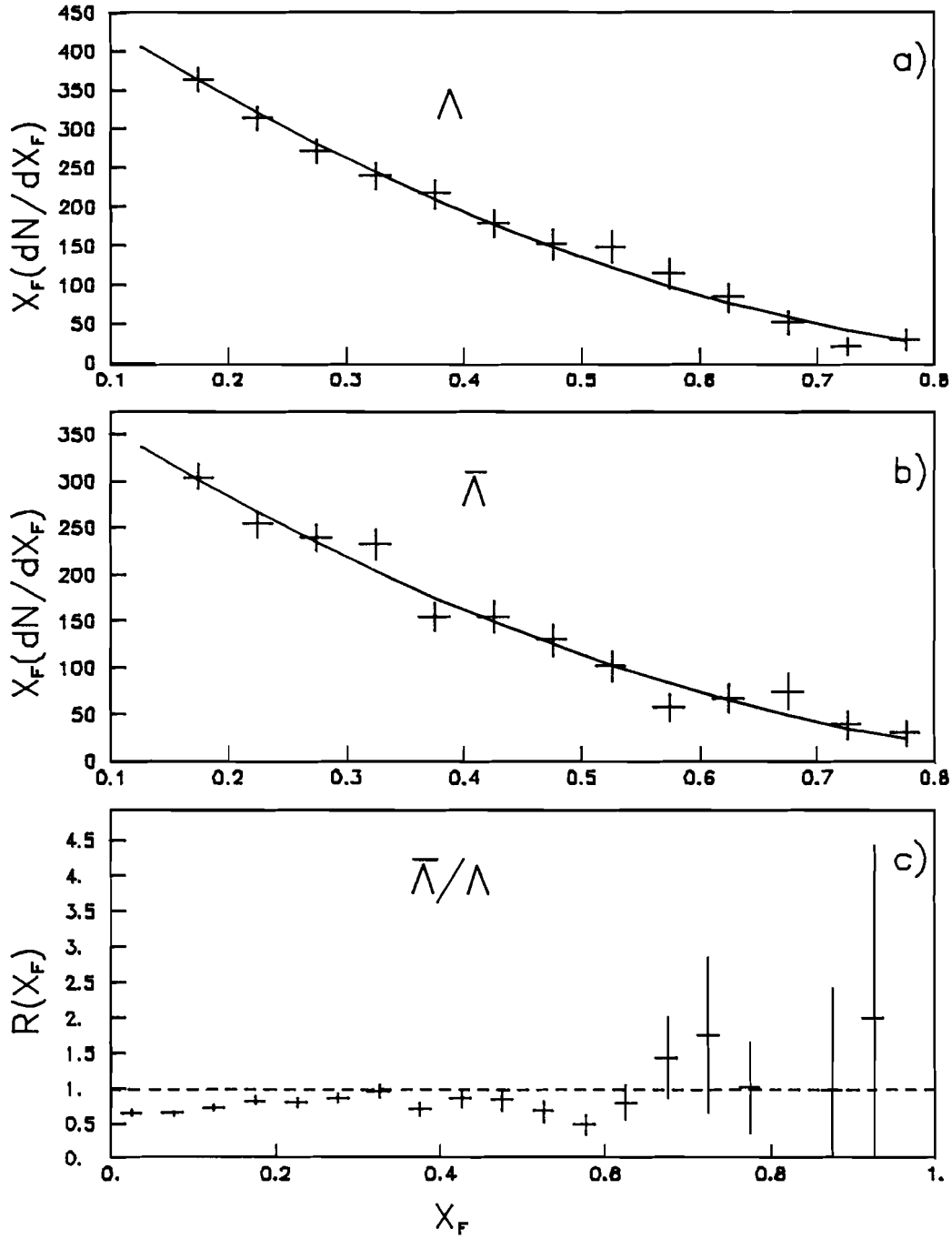

Fig. 3.2.1: The invariant X_F distributions for (a) Λ, (b) $\bar{\Lambda}$ and (c) the $\bar{\Lambda}$ to Λ ratio.

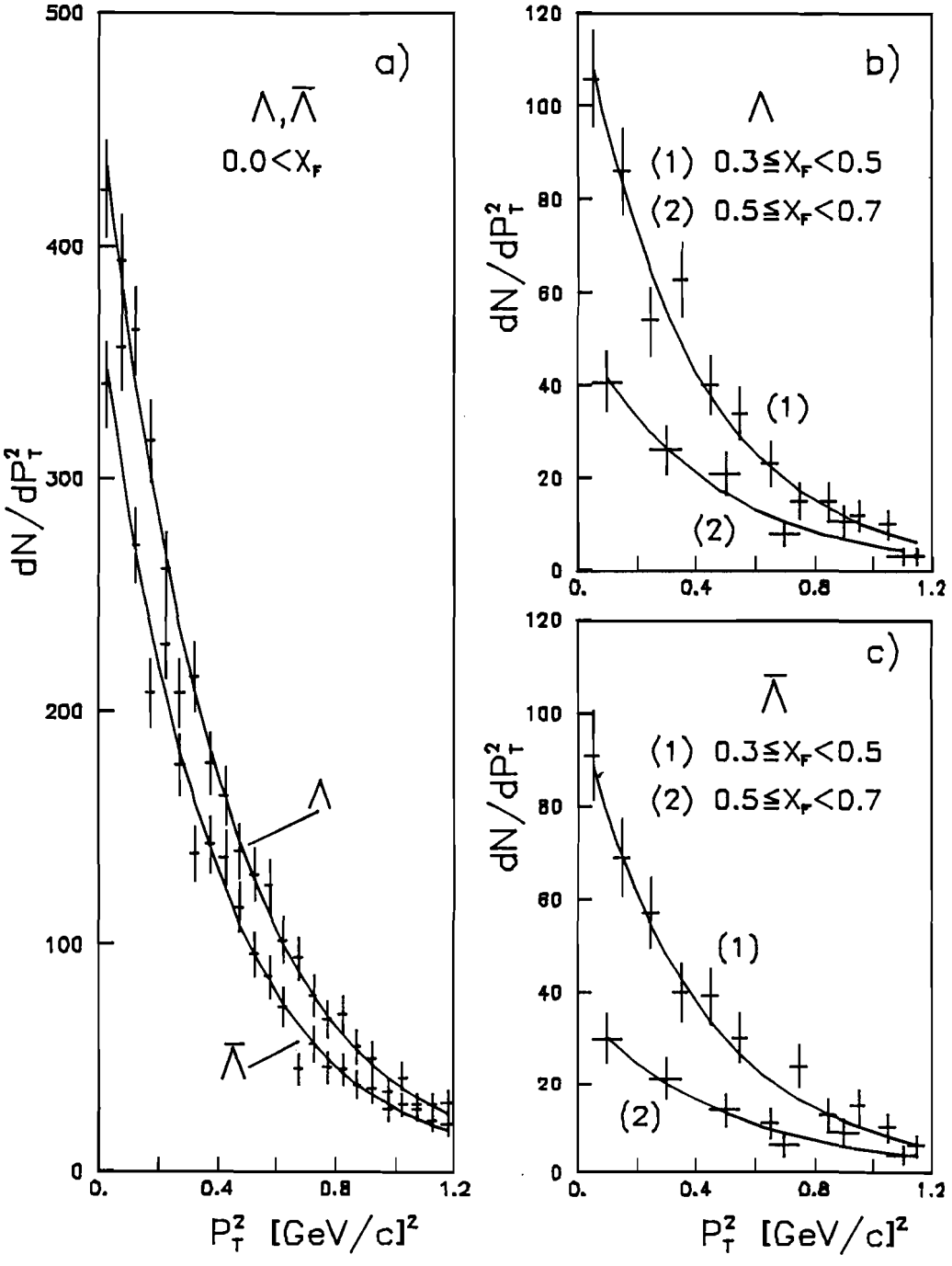

Fig. 3.2.2: The P_T^2 distribution for (a) $X_F > 0$ for $\bar{\Lambda}$ and Λ, (b) $0.3 \leq X_F < 0.5$ and $0.5 \leq X_F < 0.7$ for Λ and (c) $0.3 \leq X_F < 0.5$ and $0.5 \leq X_F < 0.7$ for $\bar{\Lambda}$.

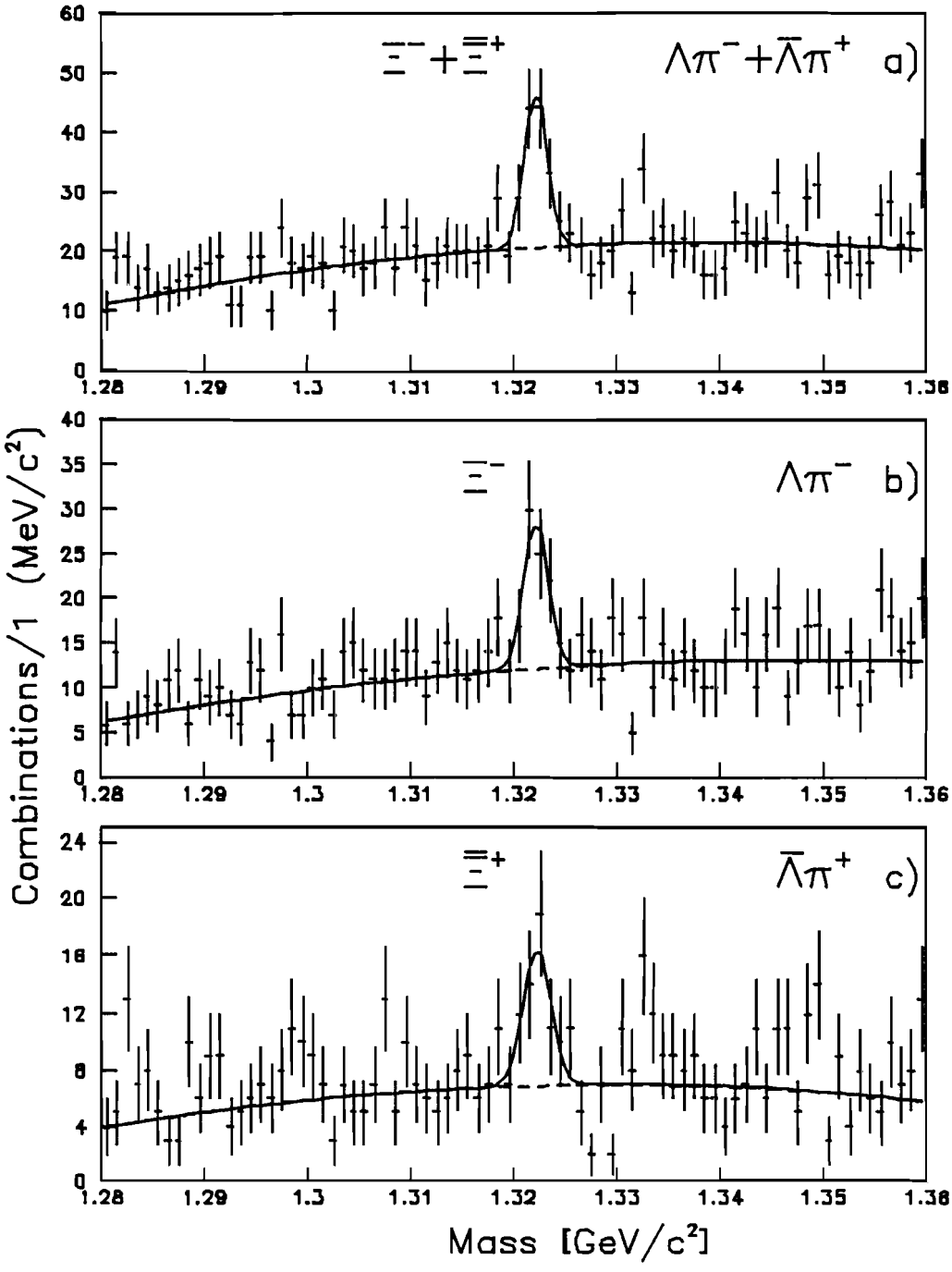

Fig. 3.2.3: Mass spectra in region Ξ(1321) for (a) $\Lambda\pi^- + \bar{\Lambda}\pi^+$, (b) $\Lambda\pi^-$ (c) $\bar{\Lambda}\pi^+$.

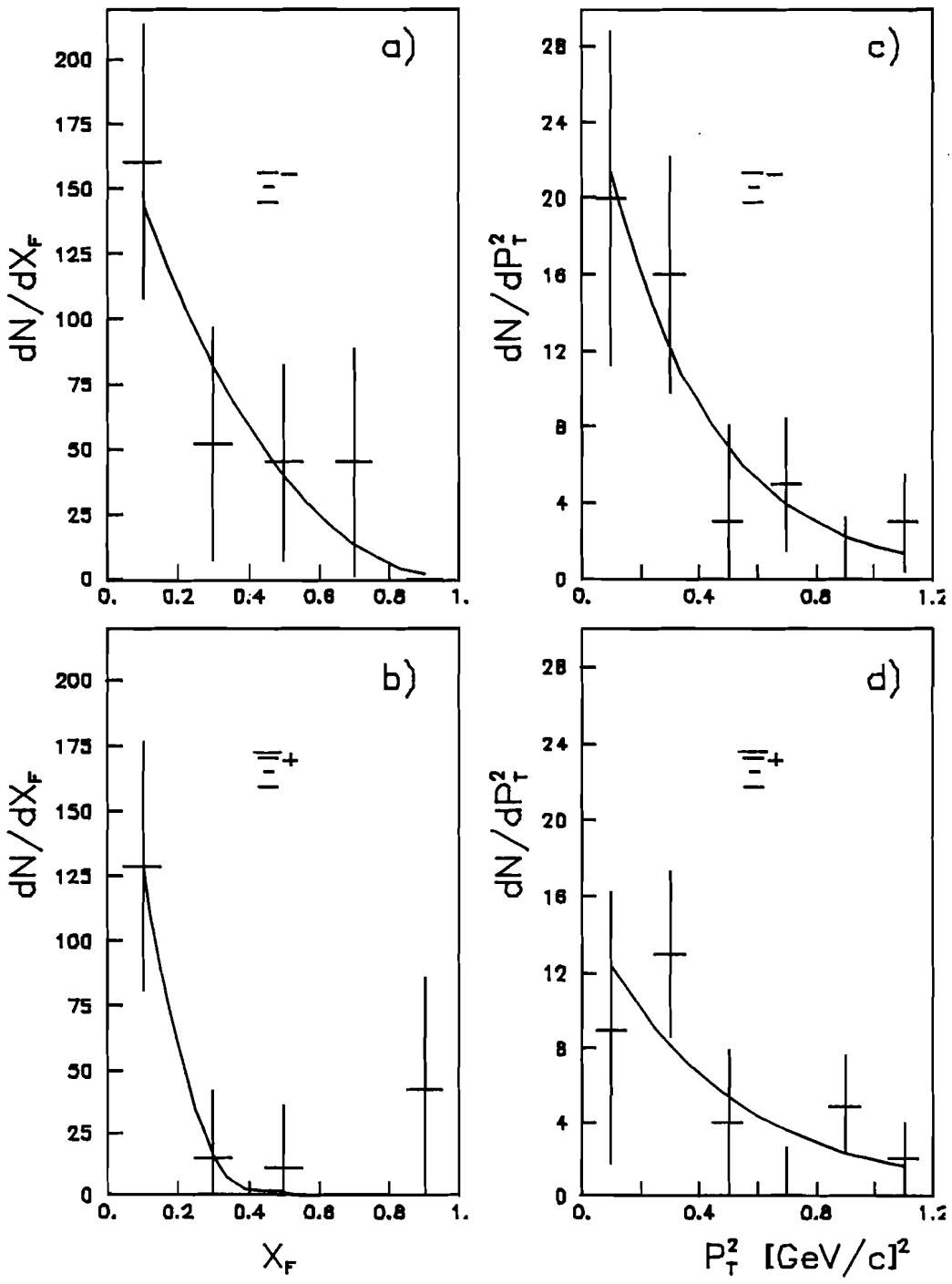

Fig. 3.2.4: The X_F distributions for (a) Ξ^-, (b) $\bar{\Xi}^+$ and the P_T^2 distributions for (c) Ξ^- and (d) $\bar{\Xi}^+$.

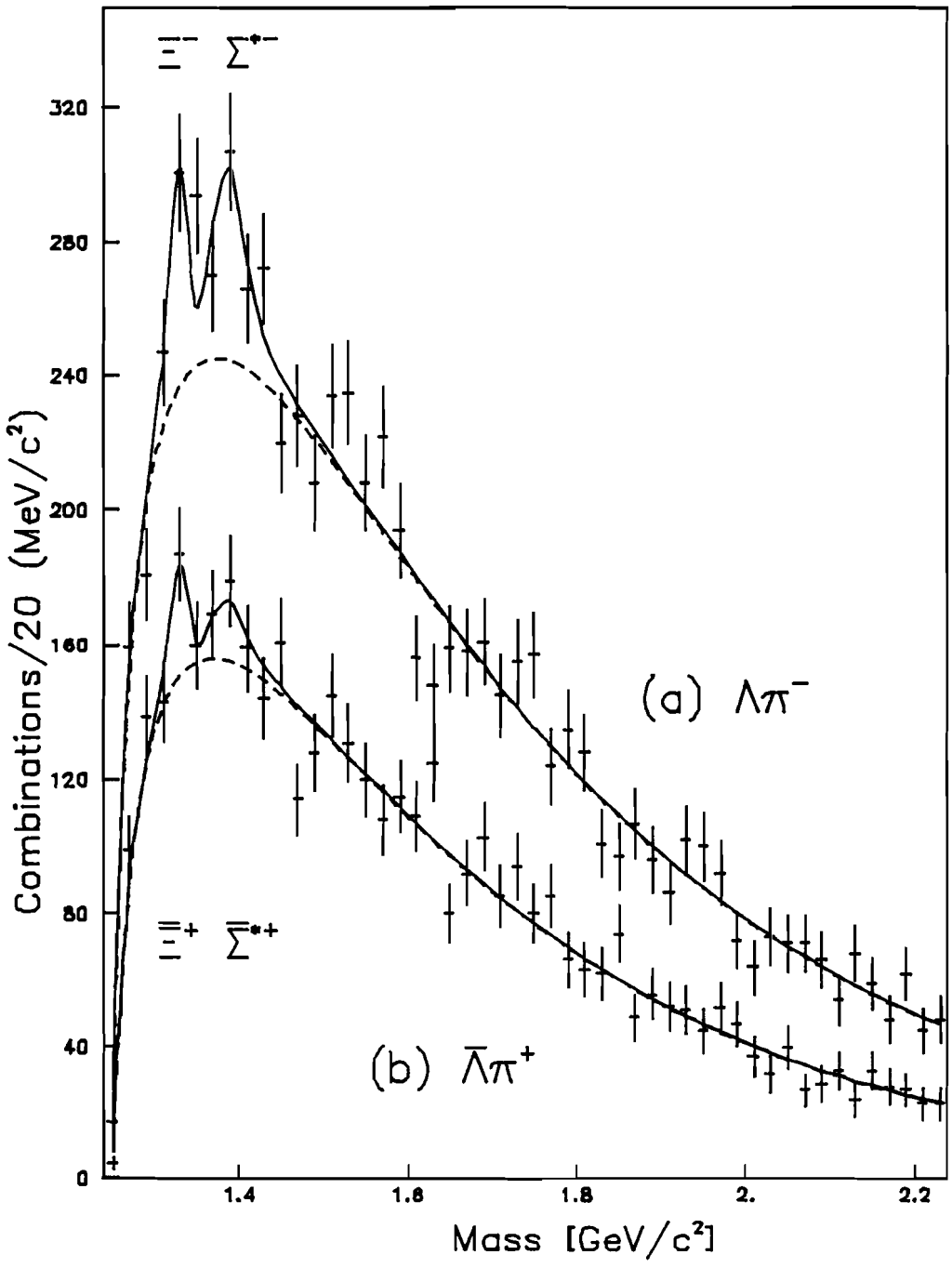

Fig. 3.2.5: Mass spectra for (a) $\Lambda\pi^-$ and (b) $\bar{\Lambda}\pi^+$.

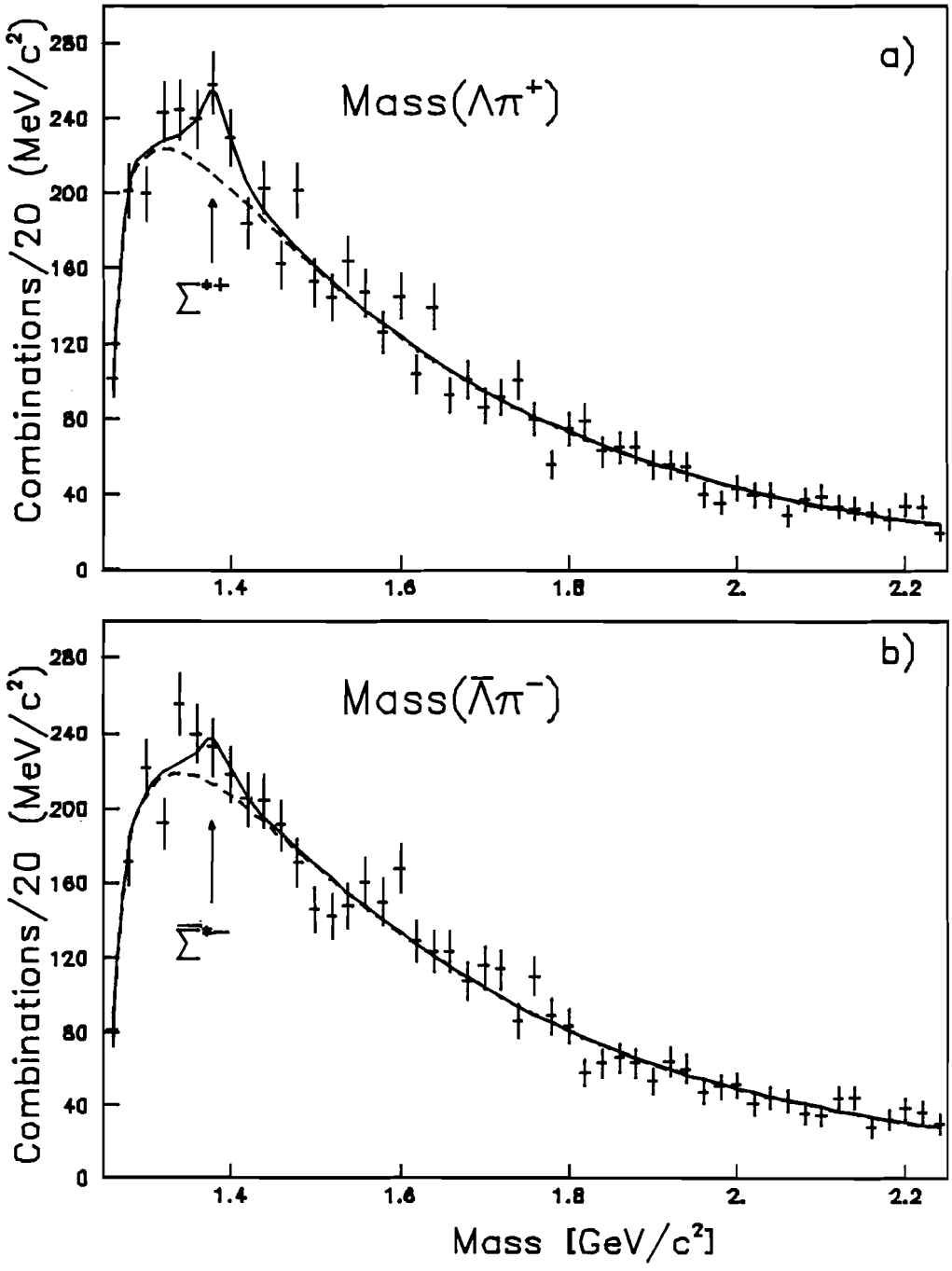

Fig. 3.2.6: Mass spectra for (a) $\Lambda\pi^+$ and (b) $\bar{\Lambda}\pi^-$.

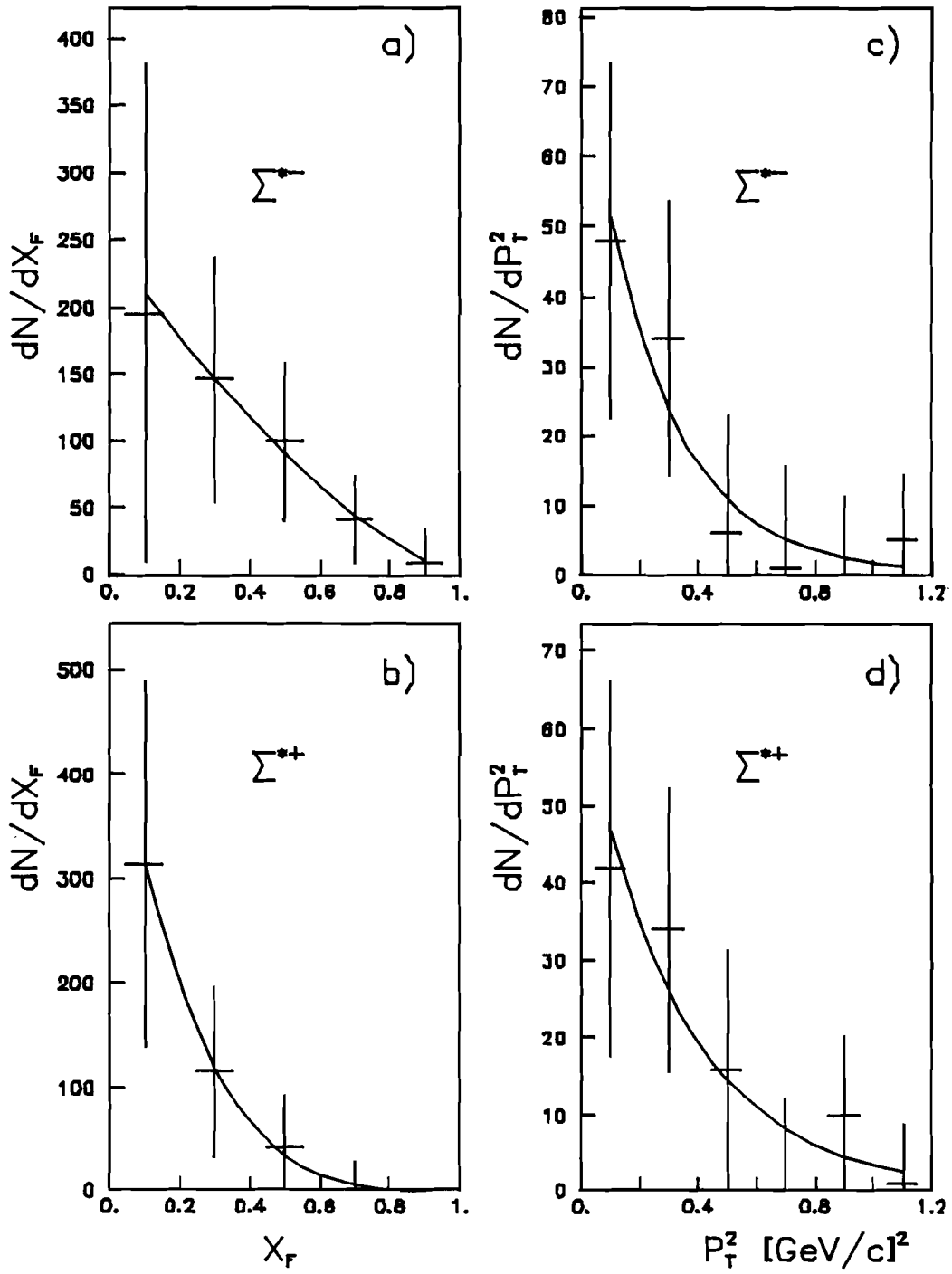

Fig. 3.2.7: The X_F distribution for (a) Σ^{*-}, (b) Σ^{*+} and the P_T^2 distributions for (c) Σ^{*-} and (d) Σ^{*+}.

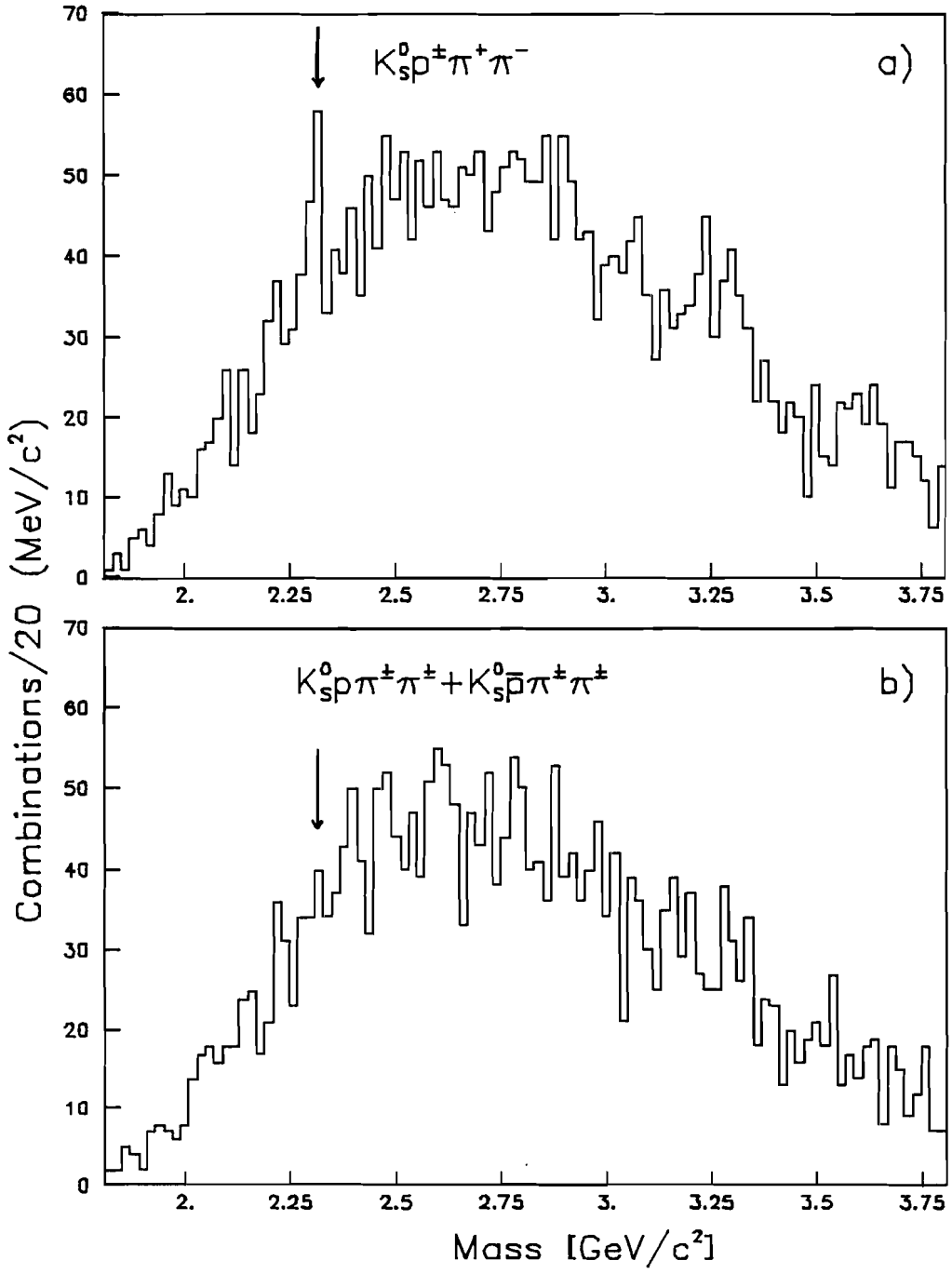

Fig. 4.1.1: Mass spectra of (a) $K^o_S p^\pm \pi^+ \pi^-$ and (b) $K^o_S p \pi^\pm \pi^\pm$ + $K^o_S p^- \pi^\pm \pi^\pm$.

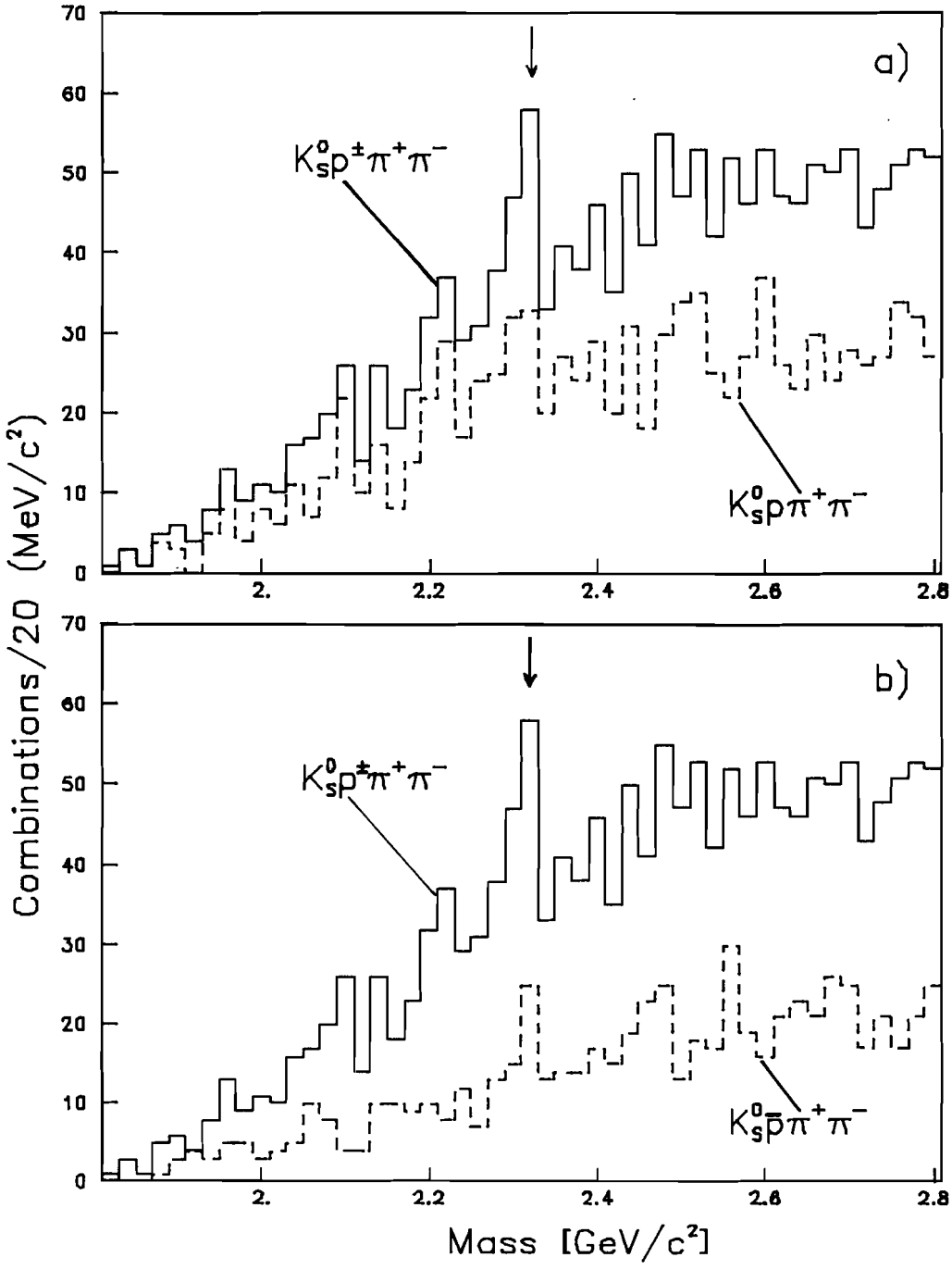

Fig. 4.1.2: Mass spectra of (a) $K^o_S p^\pm \pi^+ \pi^-$ and $K^o_S p \pi^+ \pi^-$ and (b) $K^o_S p^\pm \pi^+ \pi^-$ and $K^o_S \bar{p} \pi^+ \pi^-$.

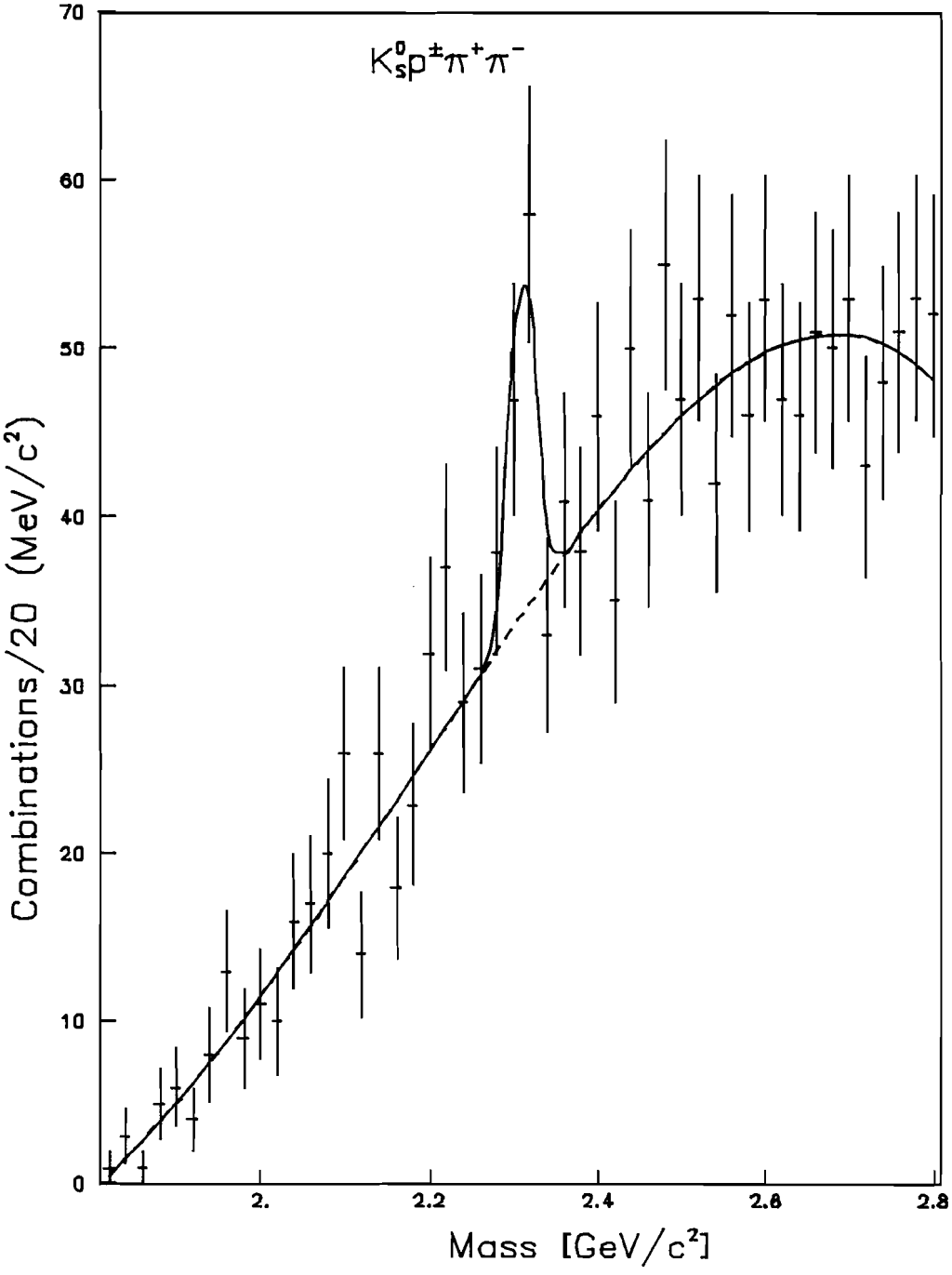

Fig. 4.1.3: The $K^o_S p^\pm \pi^+ \pi^-$ mass spectrum.

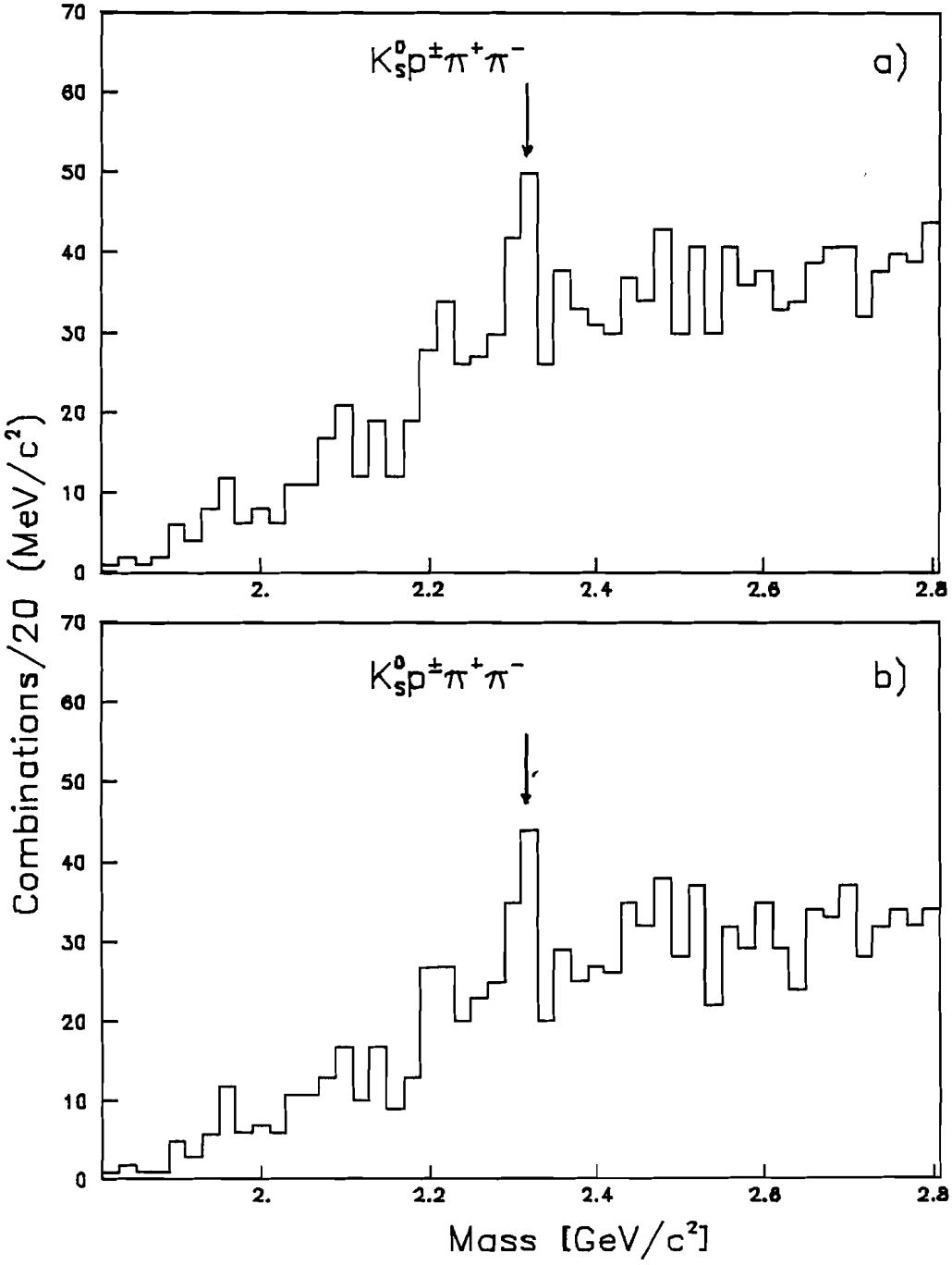

Fig. 4.1.4: The $K^0_s p^\pm \pi^+ \pi^-$ mass spectra for protons from momentum regions (a) 23.5-38.8GeV/c and (b) 25.0-38.8GeV/c.

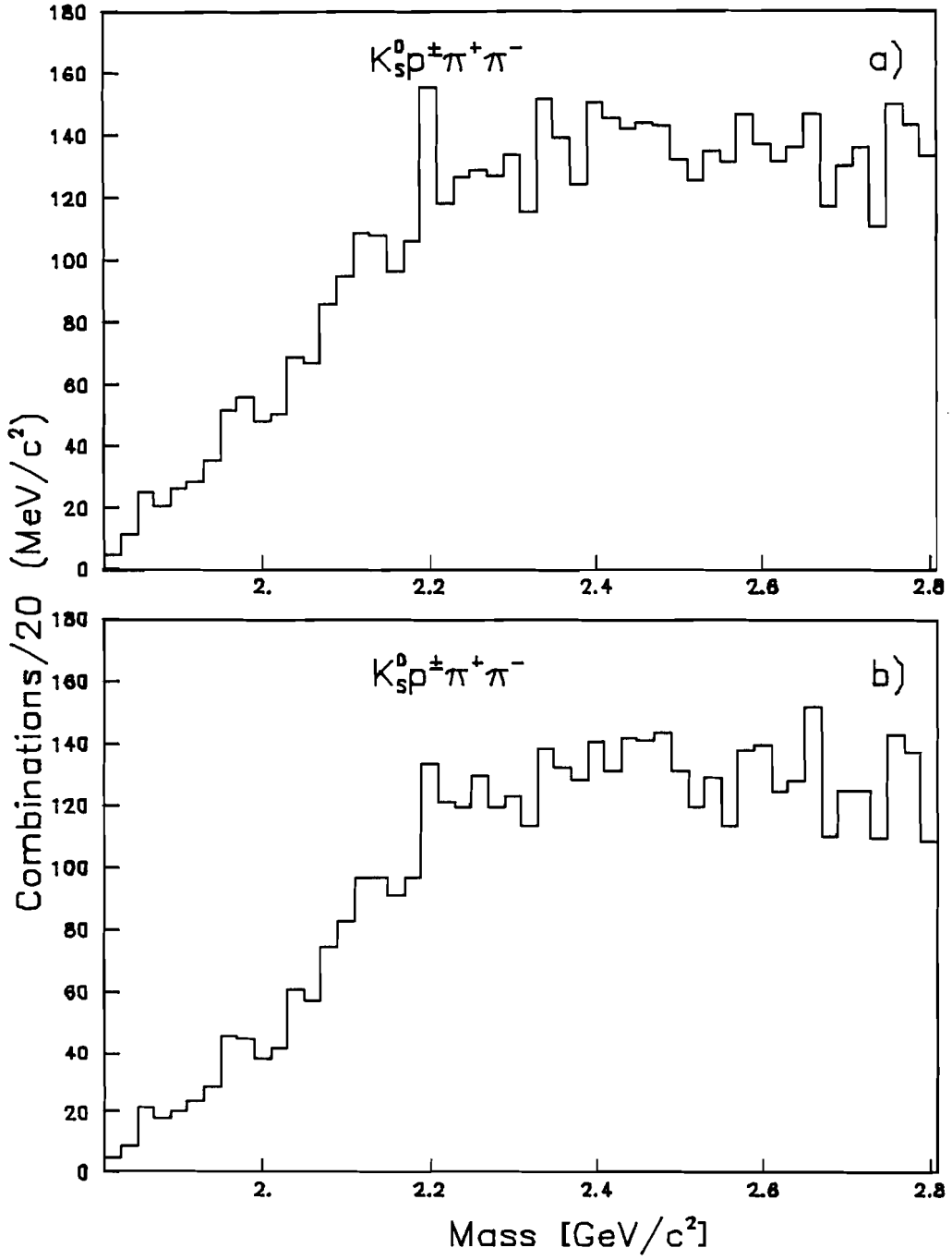

Fig. 4.1.5: The $K_S^0 p^{\pm}\pi^+\pi^-$ mass spectra for protons as the particles produced light with momentum between (a) 20.0-38.8GeV/c and (b) 23.5-38.8GeV/c.

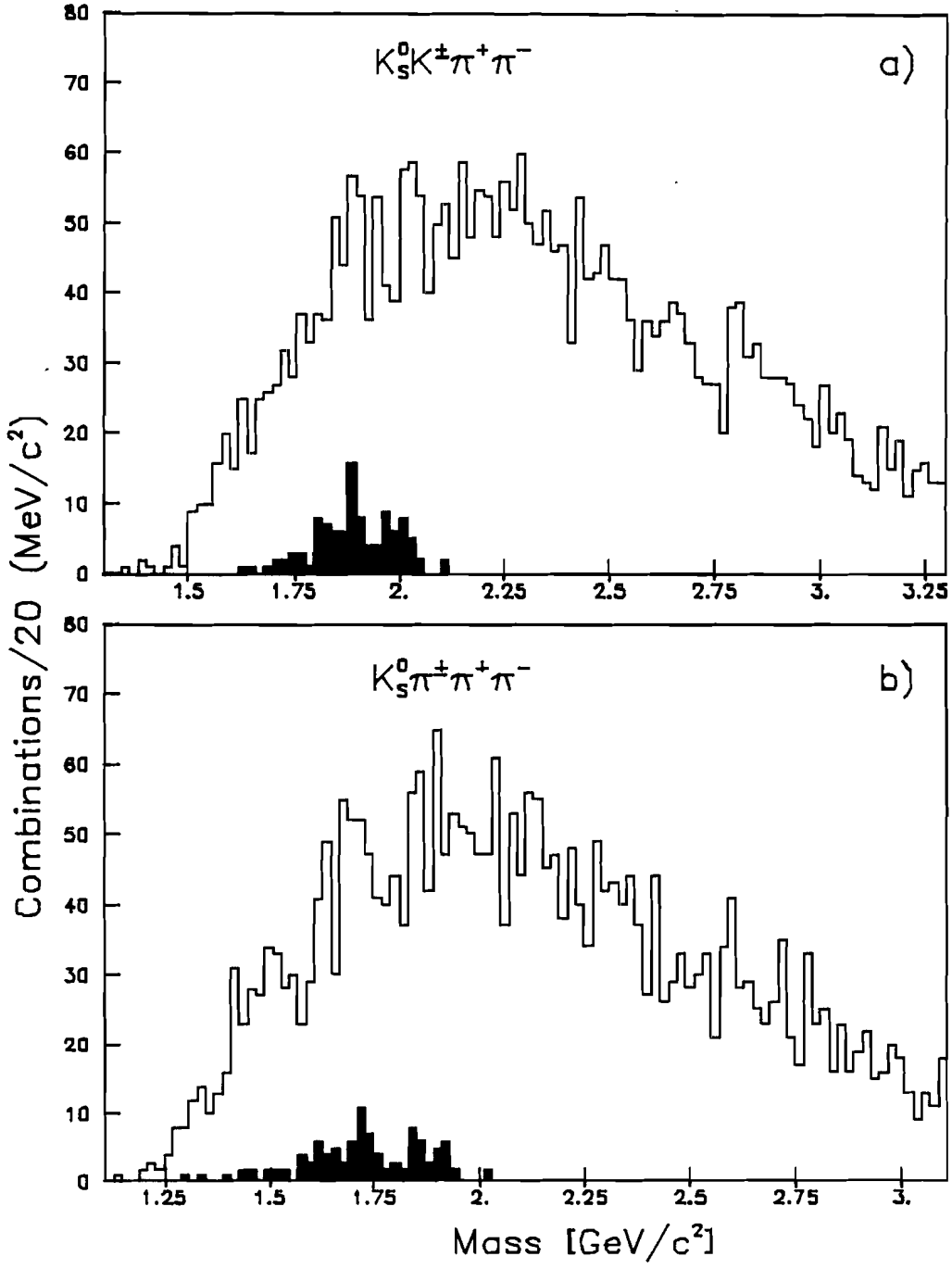

Fig. 4.1.6: The mass spectra of (a) $K_S^0K^{\pm}\pi^+\pi^-$ redefining the proton as a kaon and (b) $K_S^0\pi^{\pm}\pi^+\pi^-$ redefining the proton as a pion.

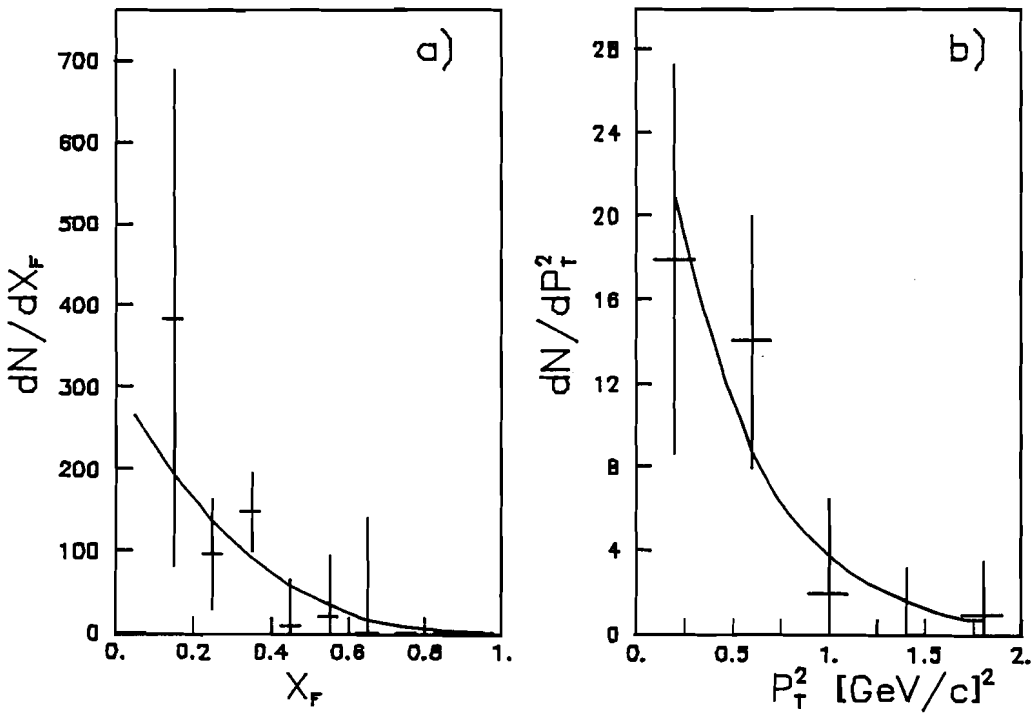

Fig. 4.1.7: The $\Lambda_c/\bar{\Lambda}_c$ (a) P_T^2 and (b) X_F distribution.

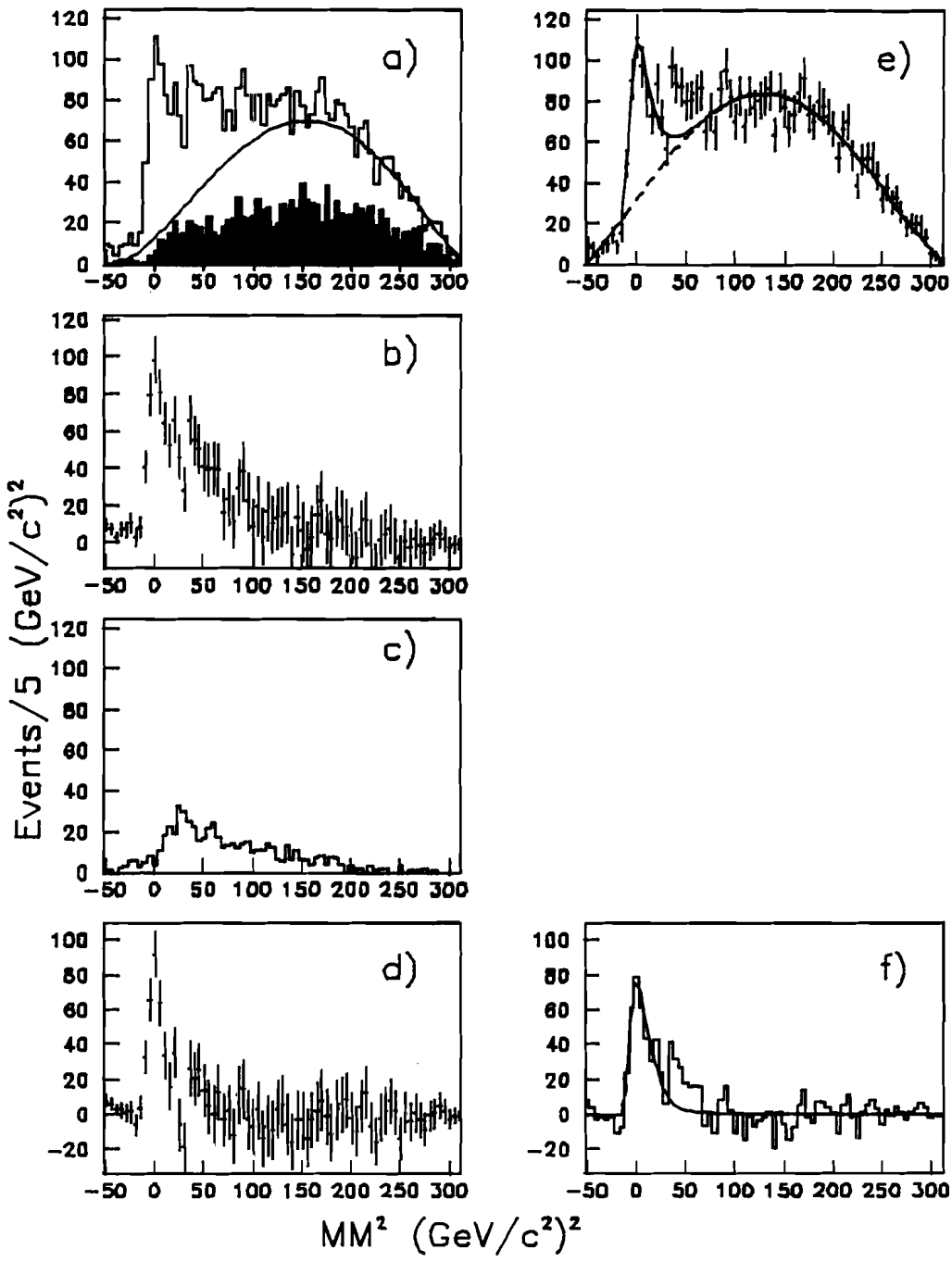

Fig. A.1: The analysis of diffraction production $\pi^- \to K^0_S \pi^+ \pi^- \pi^-$. Explanations in text.